JEM Journal of Experimental Medicine

ARTICLE

FNIP1 regulates adipocyte browning and systemic glucose homeostasis in mice by shaping intracellular calcium dynamics

Yujing Yin[1*], Dengqiu Xu[1*], Yan Mao[1*], Liwei Xiao[1], Zongchao Sun[1], Jing Liu[1], Danxia Zhou[1], Zhisheng Xu[1], Lin Liu[1], Tingting Fu[1], Chenyun Ding[1], Qiqi Guo[1], Wanping Sun[1], Zheng Zhou[1], Likun Yang[1], Yuhuan Jia[1], Xinyi Chen[1], and Zhenji Gan[1,2,3]

Metabolically beneficial beige adipocytes offer tremendous potential to combat metabolic diseases. The folliculin interacting protein 1 (FNIP1) is implicated in controlling cellular metabolism via AMPK and mTORC1. However, whether and how FNIP1 regulates adipocyte browning is unclear. Here, we demonstrate that FNIP1 plays a critical role in controlling adipocyte browning and systemic glucose homeostasis. Adipocyte-specific ablation of FNIP1 promotes a broad thermogenic remodeling of adipocytes, including increased UCP1 levels, high mitochondrial content, and augmented capacity for mitochondrial respiration. Mechanistically, FNIP1 binds to and promotes the activity of SERCA, a main Ca^{2+} pump responsible for cytosolic Ca^{2+} removal. Loss of FNIP1 resulted in enhanced intracellular Ca^{2+} signals and consequential activation of Ca^{2+}-dependent thermogenic program in adipocytes. Furthermore, mice lacking adipocyte FNIP1 were protected against high-fat diet–induced insulin resistance and liver steatosis. Thus, these findings reveal a pivotal role of FNIP1 as a negative regulator of beige adipocyte thermogenesis and unravel an intriguing functional link between intracellular Ca^{2+} dynamics and adipocyte browning.

Introduction

Beige or "brite" adipocytes are a distinct form of uncoupling protein 1 (UCP1)–expressing adipocytes in white adipose tissue (WAT) with thermogenic capacity, similar to brown adipocytes, and these cells rapidly arise in a process known as "beiging" or "browning" in response to various external stimuli, such as cold exposure or β3-adrenergic agonist treatment (Chouchani and Kajimura, 2019; Cohen and Kajimura, 2021; Harms and Seale, 2013; Kajimura et al., 2015). Beige adipocytes exert remarkable benefits on metabolic health, and active thermogenic adipocytes present in adult humans have a molecular and functional resemblance to rodent beige adipocytes (Cypess et al., 2009; Harms and Seale, 2013; Kajimura et al., 2015; Lidell et al., 2013; Shinoda et al., 2015; Wu et al., 2012). Numerous studies have suggested that increasing the amount or activity of beige adipocytes promotes a lean and healthy metabolic phenotype (Bartelt and Heeren, 2014; Cohen and Kajimura, 2021; Harms and Seale, 2013; Kajimura et al., 2015; Kusminski et al., 2016; Seale et al., 2011). Conversely, reductions in beige fat activity are linked to obesity and insulin resistance (Cohen and Kajimura, 2021; Cohen et al., 2014; Harms and Seale, 2013; Kajimura et al., 2015; Kusminski et al., 2016). Thus, delineation of the molecular mechanisms involved in regulating WAT browning is of great interest to the development of therapeutic approaches for obesity-related insulin resistance and other comorbidities.

Folliculin interacting protein 1 (FNIP1) is an adaptor protein originally identified as a binding partner of folliculin (FLCN) and AMP-activated protein kinase (AMPK; Baba et al., 2006). Underscoring the importance of the FNIP1 in cellular metabolism, mutations in FNIP1 alter cell metabolism and cause severe B cell development defects, agammaglobulinemic, hypertrophic cardiomyopathy, and pre-excitation syndrome in humans (Niehues et al., 2020; Saettini et al., 2021). While the FNIP1 pathway has been shown to influence both cellular metabolic regulators, AMPK and mammalian target of rapamycin (mTORC1), in multiple cell types (Baba et al., 2006; Petit et al., 2013; Reyes et al., 2015; Saettini et al., 2021; Siggs et al., 2016; Tsun et al.,

[1]State Key Laboratory of Pharmaceutical Biotechnology and MOE Key Laboratory of Model Animal for Disease Study, Model Animal Research Center, Department of Spine Surgery, Nanjing Drum Tower Hospital, The Affiliated Hospital of Nanjing University Medical School, Nanjing University Medical School, Nanjing University, Nanjing, China; [2]Jiangsu Key Laboratory of Molecular Medicine, Nanjing University Medical School, Nanjing University, Nanjing, China; [3]Chemistry and Biomedicine Innovation Center, Nanjing University, Nanjing, China.

*Y. Yin, D. Xu, and Y. Mao contributed equally to this paper. Correspondence to Zhenji Gan: ganzj@nju.edu.cn.

2013; Xiao et al., 2021), many recent studies have revealed multifaceted, context-dependent functions of the FNIP1 protein in metabolic control, which has been linked to cellular signaling beyond AMPK and mTOR signaling (Manford et al., 2021; Manford et al., 2020; Woodford et al., 2016; Xiao et al., 2021). For example, recent studies have reported that FNIP1 acts as a co-chaperone that regulates the chaperone function of Hsp90 (Sager et al., 2019; Sager et al., 2018; Woodford et al., 2016). Moreover, a growing body of evidence has connected FNIP1 to a broad range of cellular processes, including mitochondrial quality control, reductive stress response, and protein stability (Manford et al., 2021; Manford et al., 2020; Woodford et al., 2016; Xiao et al., 2021). However, it has yet to be unraveled whether FNIP1 signaling is implicated in controlling adipose tissue function.

Calcium (Ca^{2+}) is fundamental to a wide variety of cellular processes, including, but not limited to, muscle contraction, gene transcription, exocytosis, and cellular metabolism, in virtually all eukaryotic cells (Arruda and Hotamisligil, 2015; Berridge et al., 2000; Giorgi et al., 2018; Raffaello et al., 2016). The ER serves as the major Ca^{2+} store and plays a vital role in maintaining intracellular Ca^{2+} homeostasis. The intracellular Ca^{2+} levels are tightly regulated by an array of Ca^{2+} channels and pumps localized at ER membrane (Arruda and Hotamisligil, 2015; Prakriya and Lewis, 2015; Raffaello et al., 2016). Specifically, the inositol-1,4,5-triphosphate receptors and ryanodine receptors (RyRs) are two Ca^{2+} release channels that transport Ca^{2+} from the ER to the cytosol upon stimulation, while the sarcoendoplasmic reticulum calcium transport ATPase (SERCA) is the sole Ca^{2+}-ATPase pump that is responsible for Ca^{2+} reuptake from the cytosol to the ER lumen (Arruda and Hotamisligil, 2015; Prakriya and Lewis, 2015; Raffaello et al., 2016). Previous studies have highlighted the importance of Ca^{2+} release and reuptake across the ER membrane in cellular metabolism (Arruda and Hotamisligil, 2015; Fu et al., 2012; Fu et al., 2011; Ikeda et al., 2017). For instance, altering SERCA activity has been shown to significantly affect cell metabolism (Arruda and Hotamisligil, 2015; Fu et al., 2012; Fu et al., 2011). Both SERCA-mediated Ca^{2+} cycling and Ca^{2+} uncoupling can lead to increased energy expenditure (Bal et al., 2012; Ikeda et al., 2017). SERCA was also found to be associated with obesity and susceptibility to diabetes in humans in a Genome Wide Association Study study (Locke et al., 2015).

In this study, we investigated the metabolic role in mice of FNIP1 signaling in thermogenic adipocytes. We generated adipocyte-specific FNIP1 knockout mice and found that FNIP1 acts as a negative regulator of beige adipocyte thermogenesis to control systemic glucose homeostasis. Mice with adipocyte-specific ablation of FNIP1 show a dramatic brown remodeling of WAT and were protected against high-fat diet–induced glucose intolerance, insulin resistance, and liver steatosis. Mechanistically, we demonstrated that FNIP1 binds to the ATP hydrolysis site of SERCA to enhance its Ca^{2+} pump activity. This limits intracellular Ca^{2+} signals and dampens the Ca^{2+}-dependent thermogenic program. Our results thus demonstrate a previously unrecognized FNIP1–SERCA–intracellular Ca^{2+} pathway that regulates WAT browning.

Results

Adipocyte-specific ablation of FNIP1 promotes browning of WAT

To investigate the importance of FNIP1 in adipose tissue in vivo, we generated adipocyte-specific FNIP1 KO mice (referred to as FNIP1 AKO) by crossing mice bearing a conditional *Fnip1* allele with introns 5 and 6 floxed (*Fnip1* lox/lox) with the adiponectin promoter–driven Cre mice (Fig. 1 A). FNIP1 AKO mice were born at normal Mendelian ratios and were grossly normal on inspection. As expected, the expression of *Fnip1* mRNA and protein levels were markedly reduced in adipose tissues of FNIP1 AKO mice compared with WT littermates, whereas the protein levels of FNIP1 remain unchanged in skeletal muscle, liver, and heart (Fig. 1 B; and Fig. S1, A and B). We next examined thermogenic remodeling in adipose tissue. Remarkably, histological characterization of inguinal WAT (iWAT) from FNIP1 AKO mice showed numerous multilocular adipocytes, a hallmark of WAT browning, whereas no obvious difference in the tissue morphology was observed in the brown fat (BAT) and epididymal WAT (eWAT) from FNIP1 AKO mice compared with WT controls (Fig. 1 C). Immunohistochemistry confirmed a dramatic increase in the number of UCP1-positive beige adipocytes in the iWAT of FNIP1 AKO mice (Fig. 1 D). The marked increase of UCP1 protein accumulation in iWAT of FNIP1 AKO mice was also confirmed by immunoblotting (Fig. 1 E).

To thoroughly analyze the metabolic changes that result from loss of adipocyte FNIP1, we performed RNA sequencing (RNA-seq) analysis on mRNA isolated from iWAT of the FNIP1 AKO mice and littermate controls. Gene ontology (GO) analysis revealed that the primary gene sets most significantly induced by deletion of FNIP1 in iWAT were mitochondria and fatty acid metabolism (Fig. 1, F and G). Gene expression validation studies demonstrated that a broad array of genes involved in thermogenic and mitochondrial oxidative programs were induced in FNIP1 AKO iWAT (Fig. 1 H). Interestingly, expression of *Ucp1* was induced more strongly (~60-fold) than other brown/beige fat genes (Fig. 1 H). Consistent with the gene expression results, immunoblotting analyses confirmed the increase of mitochondrial complex I (NDUFB8), complex III (UQCRC2), complex IV (COX4), and ATP synthase (ATP5A) proteins in FNIP1 AKO iWAT (Figs. 1 I and S1 C). In contrast to iWAT, in the BAT of FNIP1 AKO mice, the number of UCP1-positive adipocytes and expression levels of mitochondrial proteins did not differ from those of WT littermate controls (Fig. S1, D–F). These results indicate that adipocyte-specific ablation of FNIP1 results in browning of WAT, while classical BAT remains largely unaffected.

Loss of adipocyte FNIP1 leads to increased mitochondrial biogenesis and respiration in iWAT

Mitochondrial electron microscopy (EM) analysis revealed a striking increase of mitochondrial area in iWAT of FNIP1 AKO mice compared with WT controls (Fig. 2, A and B). Notably, the WT mice had few small mitochondria in iWAT, whereas the FNIP1 AKO mice had enlarged and dense mitochondria (Fig. 2, A and B). Mitochondrial DNA levels were induced in parallel with the observed morphology changes in FNIP1 AKO iWAT (Fig. 2 C).

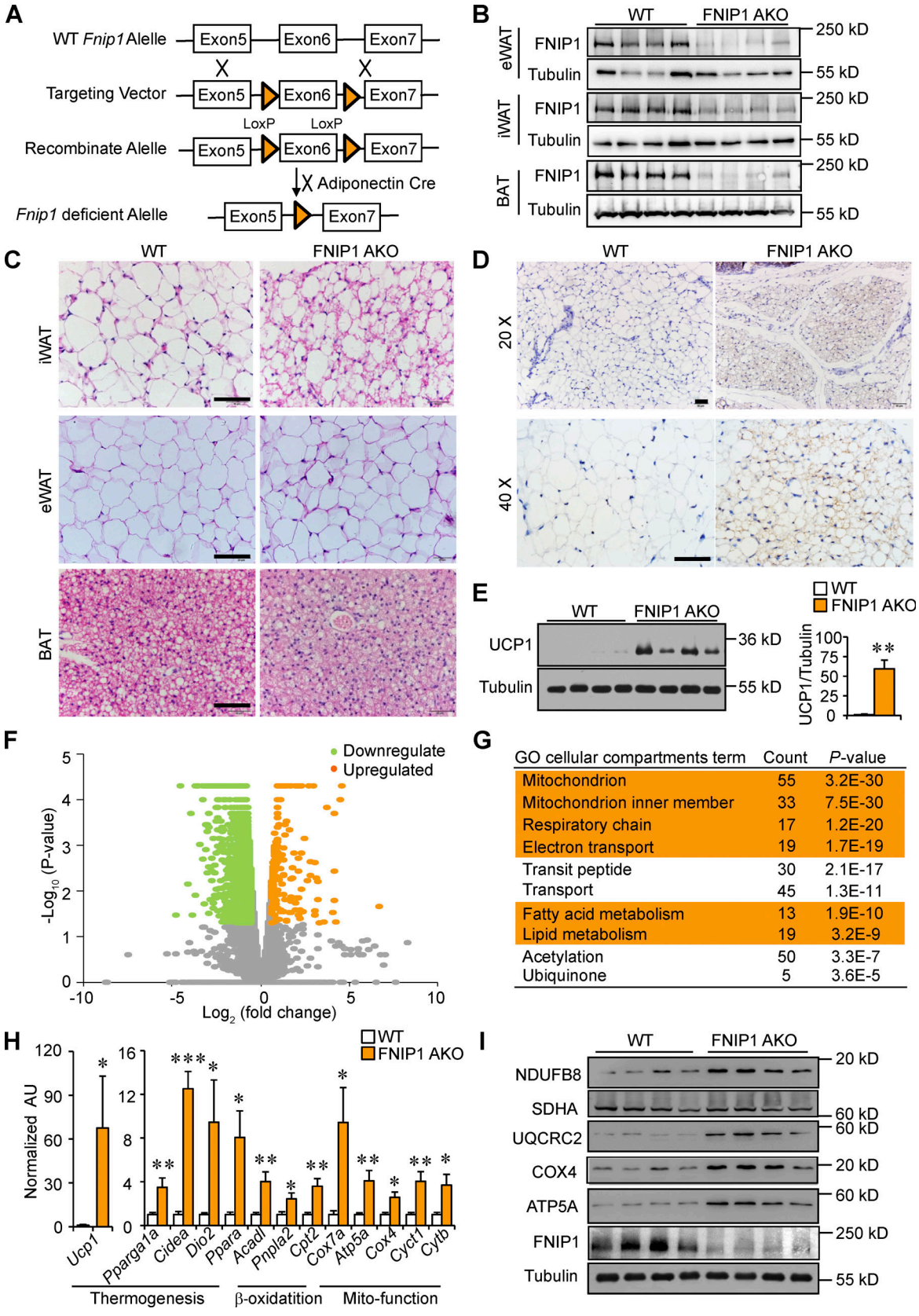

Figure 1. **Adipocyte-specific ablation of FNIP1 promotes browning of WAT. (A)** Schematic showing the generation of adipocyte-specific FNIP1 KO mice. **(B)** Representative Western blot analysis of FNIP1 protein expression in eWAT, iWAT, and BAT from indicated male mice. *n* = 8 mice per group. **(C)** H&E staining of iWAT, eWAT, and BAT of indicated male mice. Scale bar: 20 µm. *n* = 8 mice per group. **(D)** IHC staining with a UCP1-specific antibody in iWAT sections of indicated male mice. Scale bar: 50 µm (20×) or 20 µm (40×). *n* = 8 mice per group. **(E)** Left: Representative Western blot analysis of entire iWAT

lysates for male mice of the indicated genotypes. Right: Quantification of the UCP1/tubulin signal ratios. *n* = 8 mice per group. **(F)** Volcano plot showing fold changes versus P values for analyzed RNA-seq data generated from the iWAT of 8-wk-old male FNIP1 AKO mice compared with littermate controls (WT). Significantly upregulated genes are represented by orange dots, whereas downregulated genes are represented by green dots. **(G)** GO enrichment analysis of gene transcripts upregulated in male FNIP1 AKO iWAT. **(H)** Expression of genes (qRT-PCR) involved in the thermogenic and mitochondrial oxidative program in iWAT from the indicated male mice. *n* = 4–6 mice per group. **(I)** Representative Western blot analysis of entire iWAT lysates for male mice of the indicated genotypes. *n* = 11–12 mice per group. Values represent mean ± SEM. *, P < 0.05; **, P < 0.01; ***, P < 0.001. P value was determined using two-tailed unpaired Student's *t*-test. Data are representative of two (B, C, D, and H) or three independent experiments (E and I). Source data are available for this figure: SourceData F1.

Consistent with the morphology changes, pyruvate-driven mitochondrial respiration rates were significantly higher in iWAT of FNIP1 AKO mice compared with those in WT controls (Fig. 2 D). Together, these results demonstrate that loss of FNIP1 in iWAT leads to marked mitochondrial biogenesis and augmented mitochondrial respiration capacity, suggesting a broad brown remodeling of iWAT.

We next evaluated the functional consequences of marked browning of iWAT in FNIP1 AKO mice. Compared with WT littermate controls, FNIP1 AKO mice showed no difference in body weight, food intake, or locomotor activity on standard chow (Figs. 2 E and S1, G–I). FNIP1 AKO mice also had similar baseline respiratory activity and similar baseline respiratory exchange ratio (RER) as WT mice (Figs. 2, F and G; and S1 J). We thus tested the response of FNIP1 AKO mice on adrenergic stimulation, and we performed intraperitoneal injections of CL316,243 (CL) in mice and measured respiratory activity. Injection of CL induced a rapid and sustained increase in energy expenditure in WT mice. The activation of CL-induced oxygen consumption, carbon dioxide production, and heat production were all significantly increased in FNIP1 AKO mice of both sexes compared with WT controls (Figs. 2, H–K; and S2, A–D), indicating that loss of adipocyte FNIP1 enhances adrenergic thermogenesis in fat. Thermogenesis is activated to preserve body temperature to counteract the cold environment. We also tested the ability of FNIP1 AKO mice to tolerate acute cold exposure under different nutritional statuses. Relative to littermate controls, FNIP1 AKO mice showed similar cold tolerance in the fed state (Fig. S2 E). WT mice showed a rapid drop in core body temperature, especially in the fasting state during cold exposure (Figs. 2 L and S2 F). However, the body temperature of FNIP1 AKO mice of both sexes dropped at significantly slower rates than WT control mice (Figs. 2 L and S2 F), suggesting that loss of adipocyte FNIP1 influences cold-induced thermogenesis during fasting. Taken together, these results demonstrate that FNIP1 is a negative regulator of adaptive thermogenesis and energy expenditure.

FNIP1 interacts with ER Ca^{2+}-ATPase SERCA

We next sought to dissect the mechanism involved in the suppression of WAT thermogenic remodeling by FNIP1. It has been shown that FNIP1 regulates AMPK and mTORC1 signaling in several cell types (Baba et al., 2006; Petit et al., 2013; Siggs et al., 2016; Tsun et al., 2013; Xiao et al., 2021). We thus examined whether FNIP1 influences AMPK and mTOR signaling in adipocytes. Interestingly, Western blot demonstrated that levels of phosphorylated AMPK (Thr172), acetyl-CoA carboxylase (ACC), as well as downstream products of mTORC1 activation, including phosphorylated ribosomal S6 protein kinase (p-S6K) and ribosomal S6 protein (p-S6), were not different in the iWAT and BAT of the FNIP1 AKO mice compared with WT controls (Fig. 3, A–D), suggesting that differences in thermogenic programming between WT and FNIP1 AKO mice are not due to altered AMPK or mTORC1 signaling. We also took advantage of our previously generated FNIP1 KO mice and isolated adipose progenitors from iWAT of FNIP1 KO and WT mice. Cells were then induced to undergo adipocyte differentiation. Adipocytes derived from FNIP1 KO iWAT differentiated normally, suggesting that FNIP1 deletion did not influence adipocyte differentiation (Fig. 3, E and F). Notably, no changes in AMPK and mTORC1 signaling were observed in FNIP1 KO adipocytes compared with WT controls (Fig. 3 G and H). Moreover, no change in amino acids–induced phosphorylated S6 was observed in FNIP1 KO adipocytes (Fig. 3 I). These data suggest that FNIP1 affects cellular respiration without affecting AMPK and mTORC1 signaling in adipocytes.

Via immunoprecipitation (IP) and mass spectrometry (MS) analysis with muscle lysates from our previously generated *Fnip1*^{Tg} mice (Fig. S3, A and B), we identified that SERCA2, an ER Ca^{2+} channel known to affect cellular metabolism (Arruda and Hotamisligil, 2015; Bal et al., 2012; Bi et al., 2014; Fu et al., 2012; Fu et al., 2011; Ikeda et al., 2017; Periasamy et al., 2017; Verkerke et al., 2019), is able to interact and precipitate with FNIP1 (Fig. S3 A). Of particular interest is that the binding affinity of SERCA2 to FNIP1 appears to be much stronger than that of FLCN and AMPK, known interacting partners of FNIP1 (Baba et al., 2006; Fig. S3 B). SERCA is the solely Ca^{2+} influx pump that has been shown to regulate intercellular Ca^{2+} dynamics, raising the intriguing possibility that intracellular Ca^{2+} is involved in regulating the browning of WAT. To provide direct support for this notion, we used a mouse model that allowed us to monitor Ca^{2+} activity in adipose tissue in vivo. In brief, transgenic mice express a Ca^{2+} indicator GCaMP6f protein, thereby Ca^{2+} activity in the adipose tissue can be quantified by two-photon microscopy imaging (Fig. 4 A). As shown in Fig. 4, B and C, injection of norepinephrine (NE) elicited an immediate and robust increase in intracellular Ca^{2+} levels in the iWAT. Notably, NE stimulation generated a quick Ca^{2+} burst and reached a maximum within ∼1 min, then gradually reduced to near the basal level (Fig. 4, B and C; and Video 1). These data demonstrate the dynamic change of intracellular Ca^{2+} signals during NE-stimulated thermogenic remodeling in WAT in vivo. We also performed Ca^{2+} imaging studies with the GCaMP6f reporter system in isolated primary white adipocytes following exposure to NE. Consistent with previous observations in brown or beige adipocytes (Ikeda et al., 2017; Lee et al., 1993), quantitative microscopy of the GCaMP6f signals revealed a rapid rise of intracellular Ca^{2+} levels in differentiated white adipocytes within 1 min after NE application

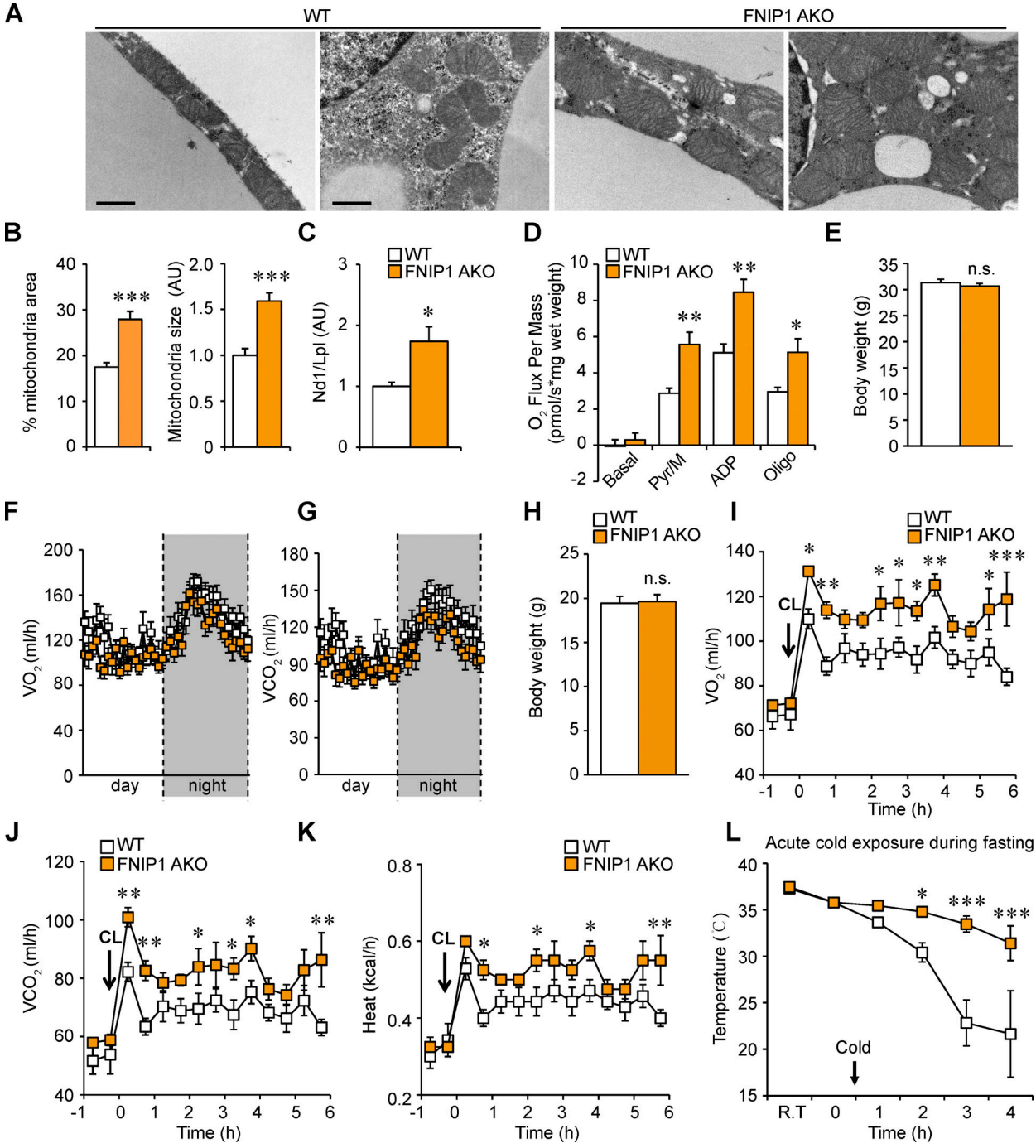

Figure 2. **Loss of adipocyte FNIP1 leads to increased mitochondrial biogenesis and respiration in iWAT. (A)** Representative electron micrographs of the iWAT showing mitochondria in sections from indicated male mice. Scale bar: 1 µm. *n* = 4 mice per group. **(B)** Percentage of mitochondrial area and mitochondrial size were quantified from the indicated male mice. *n* = 4 mice per group. 11–12 electron micrographs from each group were measured. **(C)** Results of qPCR to determine mitochondrial DNA levels in iWAT of the indicated male mice. *n* = 6–8 mice per group. **(D)** Mitochondrial respiration rates were determined from the iWAT of the indicated male mice using pyruvate as substrates. Pyruvate/malate (Pyr/M)-stimulated, ADP-dependent respiration, and oligomycin-induced (Oligo) are shown. *n* = 8 mice per group. **(E)** Body weight of indicated chow-fed 16-wk-old male mice. *n* = 7–10 mice per group. **(F and G)** Energy expenditure rates (VO_2 and VCO_2) of chow-fed 16-wk-old male mice under basal conditions. *n* = 7–10 mice per group. **(H)** Body weight of indicated chow-fed 8-wk-old female mice. *n* = 4–7 mice per group. **(I–K)** Energy expenditure rates (VO_2, VCO_2, and heat production) of chow-fed 8-wk-old female mice after CL injection (0.5 mg/kg). *n* = 4–7 mice per group. **(L)** Rectal temperature recordings taken hourly during 4 h of cold exposure using a rectal digital probe. Notably, female mice were fasted for 12 h before cold-exposure experiments. *n* = 7–9 mice per group. Values represent mean ± SEM. *, P < 0.05; **, P < 0.01; ***, P < 0.001. P value was determined using two-tailed unpaired Student's *t*-test (B, C, D, E, and H), or two-way ANOVA and Fisher's LSD post-hoc test (F, G, and I–L). Data are representative of two independent experiments (A and D).

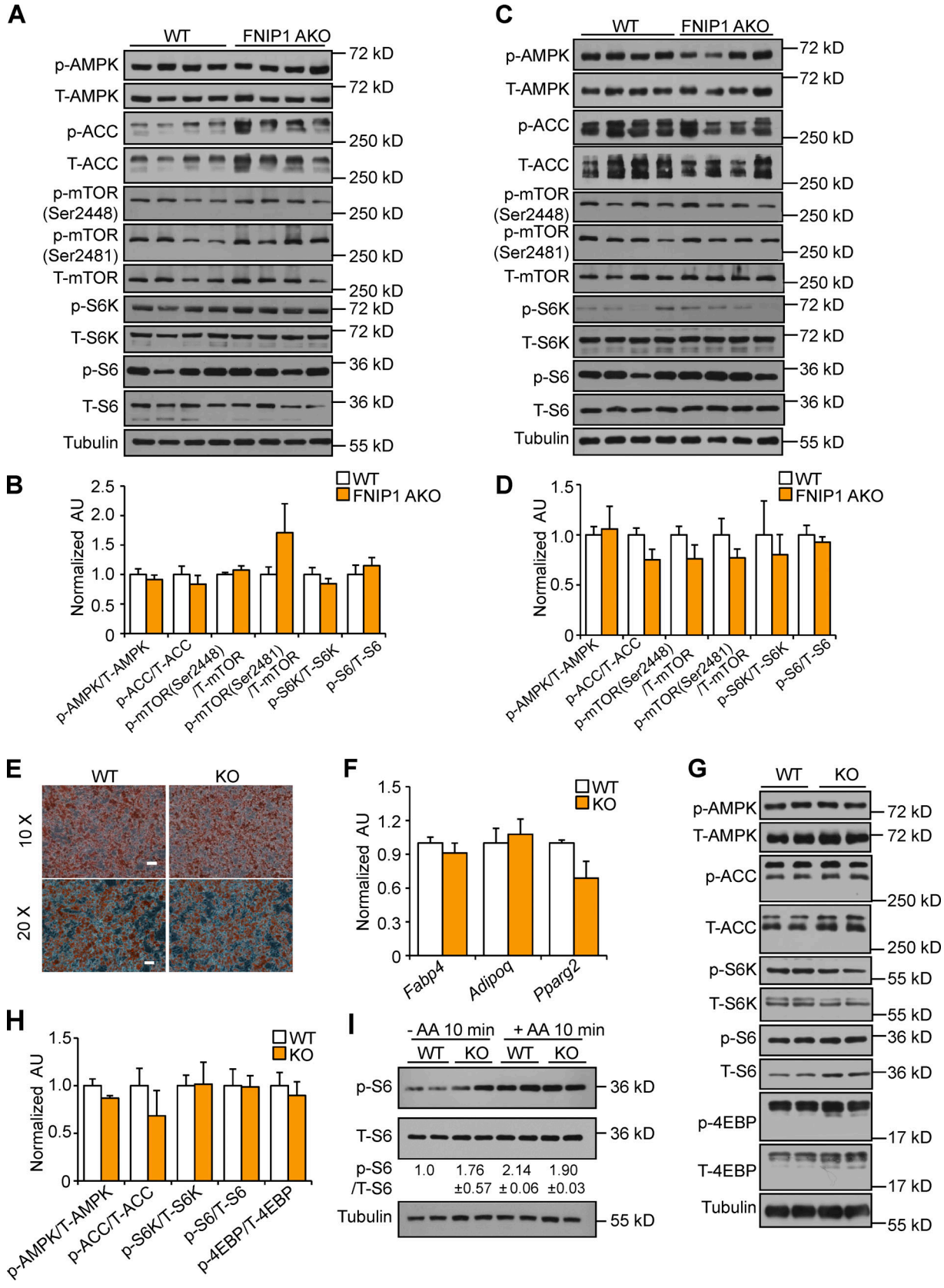

Figure 3. **Deletion of FNIP1 does not affect AMPK and mTORC1 signaling in adipocytes. (A and C)** Representative Western blot analysis of iWAT (A) or BAT (C) lysates for male mice of the indicated genotype. **(B and D)** Quantification of Western blot results in A or C. *n* = 4–13 mice per group. **(E)** Representative Oil-Red-O staining of differentiated white adipocyte isolated from iWAT of male WT and FNIP1 KO mice at low magnification (top) and at high magnification (bottom). Scale bars: 10×, 100 µm; 20×, 50 µm. *n* = 3 independent experiments. **(F)** Gene expression (qRT-PCR) in primary adipocytes. *n* = 4 independent

experiments. **(G)** Representative Western blot analysis performed with differentiated white adipocyte isolated from iWAT of male WT and FNIP1 KO mice. **(H)** Quantification of Western blot results in G. *n* = 3 independent experiments. **(I)** Representative Western blot analysis of p-S6 activation in WT and FNIP1 KO adipocytes. Cells were starved (50 min) or starved and re-stimulated with amino acids (AA) for 10 min, as indicated. Quantification of the p-S6/S6 signal ratios were presented below the corresponding bands. *n* = 3 independent experiments. Values represent mean ± SEM. P value was determined using two-tailed unpaired Student's *t*-test. Data are representative of at least three independent experiments (A, C, E–G, and I). Source data are available for this figure: SourceData F3.

(Fig. 4, D and E; and Video 2). Together, these results suggest a link between intracellular Ca^{2+} dynamics and white adipocyte thermogenic remodeling.

To verify that SERCA-mediated Ca^{2+} signals play a role in regulating white adipocyte thermogenic remodeling, we treated differentiated white adipocytes with thapsigargin (TG), a commonly used inhibitor of SERCA, which resulted in elevated intracellular Ca^{2+} levels. As expected, GCaMP6f signal intensity increased approximately threefold after TG treatment in white adipocytes (Fig. 4 F). The mRNA levels of key thermogenic genes, such as *Ucp1*, *Ppargc1a*, and *Dio2*, were all significantly increased at 4-h posttreatment with TG (Fig. 4 F). These data indicate that inhibiting SERCA activity, leading to increased intracellular Ca^{2+} levels, is indeed capable of triggering thermogenic gene programs in white adipocytes. To ascertain the role of Ca^{2+} signals in regulating adipocyte thermogenic gene program, the effects of forskolin (FSK), a cAMP signaling inducer that potently induces thermogenic gene expression, were assessed alone or together with a cell-permeant Ca^{2+} chelator, 1,2-Bis(2-aminophenoxy)ethane-N,N,N′,N′-tetraacetic acid tetrakis(acetoxymethyl ester; BAPTA-AM). As expected, FSK potently induced expression of key thermogenic genes in white adipocytes (Fig. 4 G). BAPTA-AM had no effect on basal thermogenic gene expression but markedly inhibited the FSK-mediated stimulatory effect (Fig. 4 G). Similar observations were obtained when white adipocytes were treated with the β3-adrenergic agonist CL. The mRNA expression of key thermogenic genes was induced by CL stimulation, which could be significantly attenuated by BAPTA-AM treatment (Fig. 4 H). Taken together, these results demonstrate that intracellular Ca^{2+} dynamics are necessary for thermogenic gene reprogramming in white adipocytes.

A series of co-IP studies were next conducted to confirm the interaction between FNIP1 and SERCA2. HEK293T cells were co-transfected with expression vectors for Flag-FNIP1 and HA-SERCA2b. FNIP1 was coimmunoprecipitated with SERCA2b using anti-hemagglutinin (HA) antibodies (Fig. 5 A). Using FNIP1 as the immunoprecipitation target, SERCA2b was reciprocally pulled down (Fig. 5 B). Moreover, GFP-FNIP1 and Mcherry-SERCA2b, transiently co-transfected into HEK293T cells, colocalized in the cytoplasm with a reticular pattern (Fig. 5 C). In addition, FNIP1 was also found to colocalize with the ER marker GFP-Mannosidae II (MANII), consistent with its ER SERCA2b interaction (Fig. S3 C).

Human SERCA2b protein is composed of 1,042 amino acids, which can be structurally divided into four different domains (Fig. 5 D). To identify the functional domains of SERCA2b that interact with FNIP1, we expressed Flag-tagged FNIP1 with the SERCA2b deletion variants (Fig. 5, D and E). As shown in Fig. 5 E, among deletion fragments of SERCA2b, FNIP1 was only bound to the fragment containing both the phosphorylation domain (residues 328–505, P) and nucleotide-binding domain (residues 505–680, NB), and the P deletion or the NB deletion abolished the interaction of SERCA2b with FNIP1 (Fig. 5 E). These results were of interest because the phosphorylation and nucleotide-binding domains are functionally closely related to the formation of the active site of ATP hydrolysis, which is essential for SERCA pump activity. Therefore, these results indicate a critical role of the intact active site of ATP hydrolysis in FNIP1 and SERCA2b binding. We also mapped the critical region of FNIP1 that binds to SERCA2b (Fig. 5, D and F). Analysis of FNIP1 deletion mutants revealed that the N-terminal region (amino acids 1–300) of FNIP1 is required for the interaction between SERCA2b and FNIP1 (Fig. 5, D and F). Therefore, the N-terminal region of FNIP1 binds to the ATP hydrolysis site of SERCA pump (Fig. 5 G). To further determine the in vivo physiological relevance of these interactions, co-IP studies with anti-FNIP1 antibodies were conducted with extracts of iWAT from WT mice after adrenergic stimulation. As shown in Fig. 5 H, endogenous FNIP1 and SERCA2 showed decreased interaction in iWAT after CL stimulation (Fig. 5 H), suggesting that a dissociation of FNIP1 from SERCA2 may play a role in the regulation of intracellular Ca^{2+} upon adrenergic stimulation.

FNIP1 affects SERCA activity and modulates intracellular Ca^{2+} homeostasis

We next explored the biological significance of the FNIP1–SERCA interaction. The SERCA pump depends on its ATP hydrolysis to translocate Ca^{2+}. To determine whether FNIP1 binding affects SERCA pump activity, we firstly performed SERCA ATPase activity measurements in HEK293T cells transiently expressing FNIP1 and SERCA2b. SERCA ATPase activity was measured in cell homogenates by a spectrophotometric assay using a coupled enzymatic system in the absence or presence of TG to determine SERCA-dependent and -independent activity (De Smedt et al., 1991). Remarkably, in the presence of FNIP1, significant activation of SERCA ATPase activity (approximately fourfold) was observed (Fig. 6 A). These data indicate that FNIP1 binds to the ATP hydrolysis site of SERCA2b to preserve its ATPase activity. To further affirm the regulation of SERCA pump activity by FNIP1, we performed Ca^{2+} transporting assay with purified microsomes enriched in ER membranes. Consistent with the stimulatory effect of FNIP1 on SERCA2b ATPase activity, the Ca^{2+}-transporting activity of microsomes prepared from cells overexpressing FNIP1 was higher than those isolated from control cells, indicating that FNIP1 promotes SERCA2b Ca^{2+} pump activity (Fig. 6 B). Moreover, we also monitored intracellular Ca^{2+} dynamics using Fluo-4 acetoxymethyl

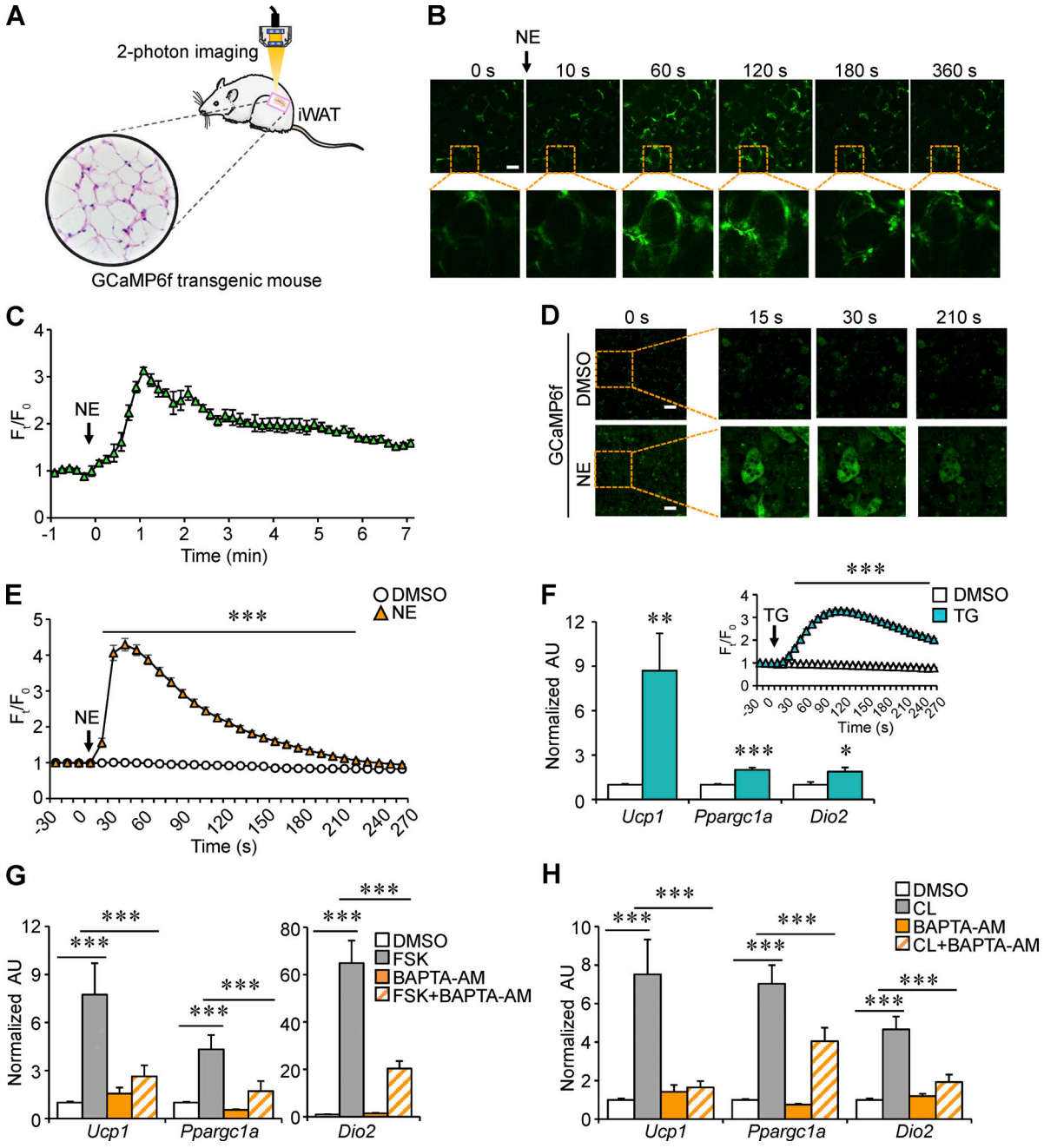

Figure 4. **Intracellular Ca^{2+} dynamics regulates thermogenic gene program in white adipocytes. (A)** Schematic showing the monitoring of Ca^{2+} activity in adipose tissue in vivo using the GCaMP6f transgenic mice. **(B)** Representative time-lapse images of iWAT of male GCaMP6f transgenic mice at different time intervals after 1 mg/kg NE stimulation. The corresponding video is included as Video 1. Scale bars: 50 µm. **(C)** Quantitative analysis of the GCaMP6f fluorescence intensity (F_t/F_0) in B. Curve depicts the measurements from four independent mice. **(D)** Representative time-lapse images of differentiated white adipocytes isolated from iWAT of male GCaMP6f transgenic mice at different time intervals after DMSO (top) or 1 µM NE stimulation (bottom). The corresponding video is included as Video 2. Scale bars: 50 µm. **(E)** Quantitative analysis of the GCaMP6f fluorescence intensity (F_t/F_0) in D. Curves depict the measurement of 100–141 cells from four independent experiments. **(F)** Gene expression (qRT-PCR) in differentiated white adipocytes. Cells were treated with 2 µM TG for 4 h. Inset: Quantitative analysis of the GCaMP6f fluorescence intensity (F_t/F_0). n = 4 independent experiments. **(G and H)** Gene expression (qRT-PCR) in differentiated white adipocytes. Cells were treated for 4 h with DMSO (vehicle), 10 µM FSK, 20 µM CL, 10 µM BAPTA-AM, FSK + BAPTA-AM, or CL + BAPTA-AM as indicated in the key. n = 4 independent experiments. Values represent mean ± SEM. *, P < 0.05; **, P < 0.01; *** P < 0.001. P value was determined using two-tailed unpaired Student's t-test (E and F) or one-way ANOVA coupled to a Fisher's LSD post-hoc test (G and H). Data are representative of four independent experiments (B–H).

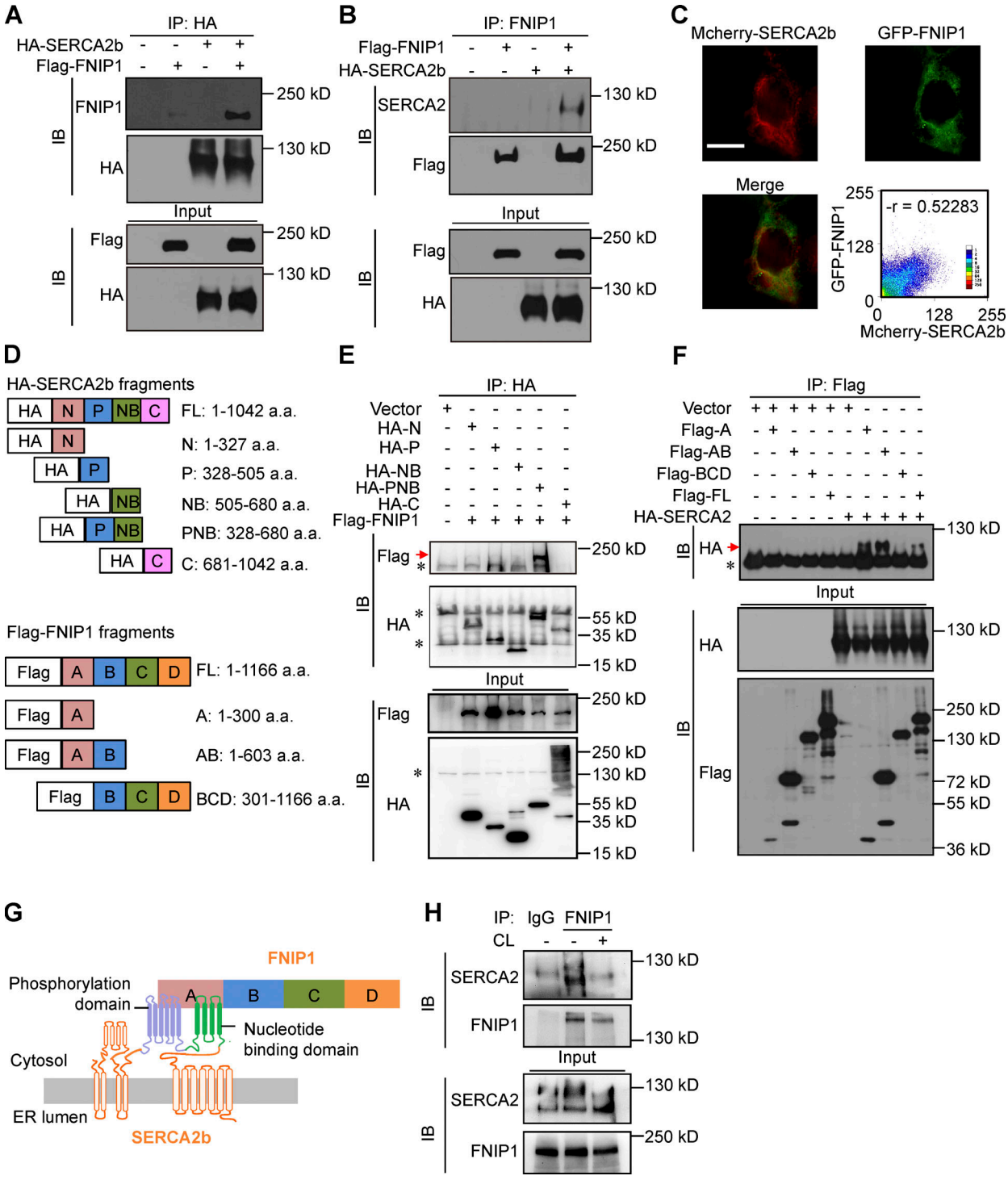

Figure 5. **FNIP1 interacts with ER Ca^{2+}-ATPase SERCA. (A and B)** Co-IP experiments were performed by co-transfecting HA-SERCA2b and Flag-FNIP1 in HEK293T cells, as indicated at the top. Extracts (input) from the HEK293T cells and proteins from the IP were analyzed by immunoblotting (IB). Representative results for co-IP are shown. *n* = 3 independent experiments. **(C)** GFP-FNIP1 and Mcherry-SERCA2b colocalized in the cytoplasm. Scale bar: 100 µm. **(D)** Top: Schematic diagrams of different HA-tagged SERCA2b constructs. Bottom: Schematic diagrams of different Flag-tagged FNIP1 constructs. a.a., amino acid. **(E)** Deletion of the P or NB region abolishes the coimmunoprecipitation of FNIP1 and SERCA2b. Representative results for co-IP are shown. *n* = 3 independent experiments. **(F)** Deletion of the A region abolishes the co-IP of SERCA2b and FNIP1. Representative results for co-IP are shown. *n* = 3 independent experiments. **(G)** The schematic depicts a proposed model for the FNIP1-SERCA2b interaction. **(H)** Co-IP of endogenous FNIP1 and SERCA2 using iWAT from male WT mice treated with NaCl or CL316,243 (1 mg/kg) for 1 h. Representative results for co-IP are shown. *n* = 3 independent experiments. Data are representative of three independent experiments (A–C, E, F, and H). Source data are available for this figure: SourceData F5.

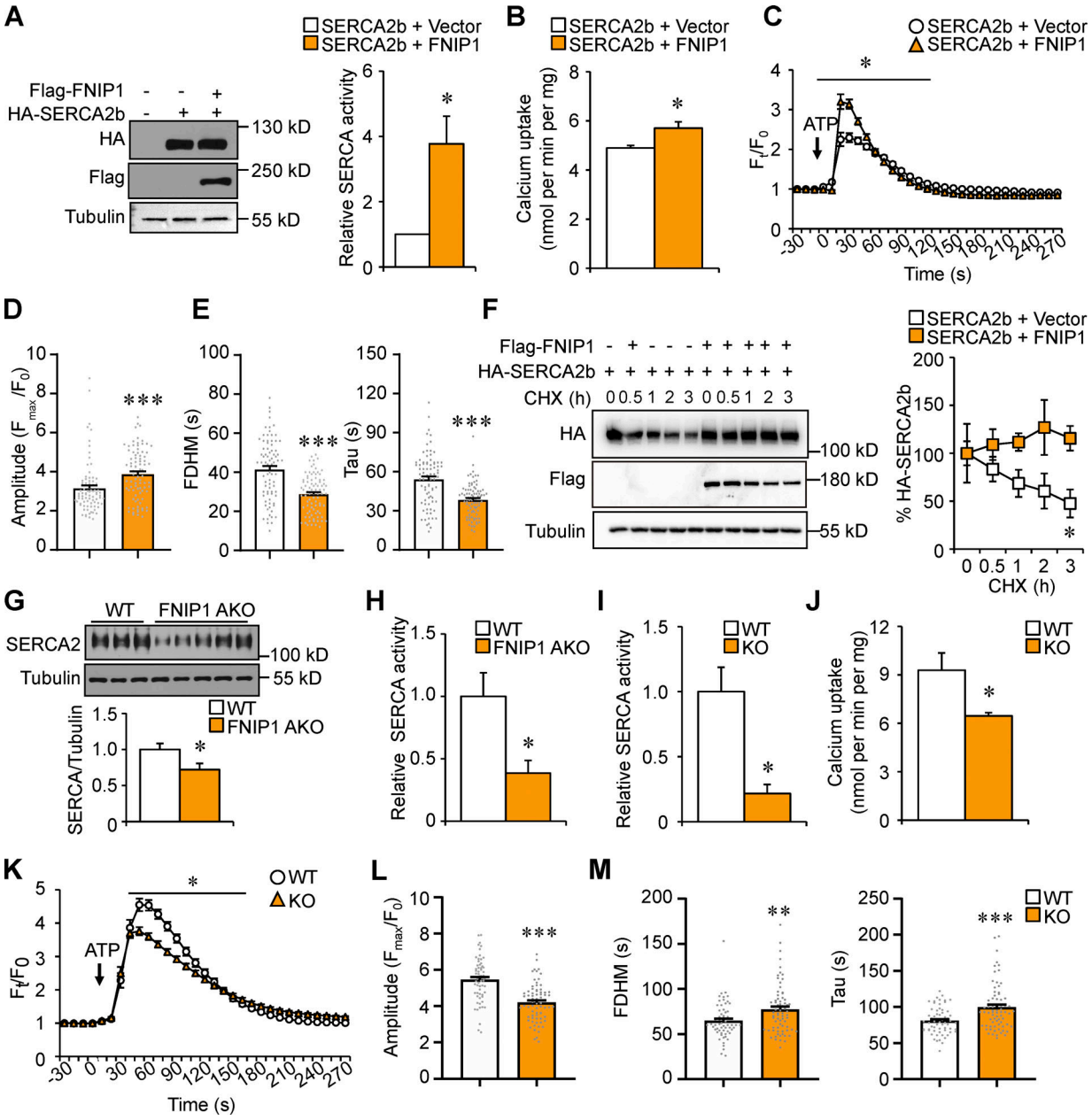

Figure 6. **FNIP1 affects SERCA activity and modulates intracellular Ca^{2+} homeostasis. (A)** Left: Western blot analysis confirms the expression of Flag-tagged FNIP1 and HA-tagged SERCA2b in indicated cells. Right: SERCA ATPase activity in HEK293T cell homogenates. *n* = 3 independent experiments. **(B)** Ca^{2+}-transporting activity of microsomes prepared from HEK293T cells expressing the indicated proteins. *n* = 4 independent experiments. **(C–E)** Ca^{2+} transients in HEK293T cells expressing mCherry-SERCA2b together with or without FNIP1 protein. Ca^{2+} dynamics were monitored using Fluo-4 AM in cells following exposure to 100 nM ATP. *n* = 81–85 cells per group from four independent experiments. Quantitative analysis of the Fluo-4 AM fluorescence intensity (F_t/F_0; C). Quantitation of amplitude (D), FDHM, and time constant Tau (E) of Ca^{2+} transients. **(F)** HEK293T cells were co-transfected with plasmids encoding HA-SERCA2b, Flag-FNIP1, or control vector. Left: CHX treatment of cells for the indicated time. Right: Quantification of the SERCA2b protein levels. *n* = 3 independent experiments. **(G)** Top: Western blot analysis of SERCA2 protein expression in iWAT of indicated male mice. Bottom: Quantification of SERCA2/Tubulin signal ratios. *n* = 10–12 mice per group. **(H)** SERCA ATPase activity in iWAT homogenates from male WT and FNIP1 AKO mice. *n* = 4–5 mice per group. **(I)** SERCA ATPase activity in cell homogenates from differentiated white adipocyte isolated from iWAT of WT and FNIP1 KO mice. *n* = 3 independent experiments. **(J)** Ca^{2+}-transporting activity of microsomes prepared from differentiated white adipocyte isolated from iWAT of male WT and FNIP1 KO mice. *n* = 4 independent experiments. **(K–M)** Ca^{2+} transients in differentiated white adipocyte isolated from iWAT of male WT and FNIP1 KO mice. Ca^{2+} dynamics were monitored using Fluo-4 AM in cells following exposure to 100 nM ATP. *n* = 62–72 cells per group from three independent experiments. Quantitative analysis of the Fluo-4 AM fluorescence intensity (F_t/F_0; K). Quantitation of amplitude (L), FDHM, and time constant Tau (M) of Ca^{2+} transients. Values represent mean ± SEM. *, P < 0.05; **, P < 0.01; ***, P < 0.001. P value was determined using two-tailed unpaired Student's *t*-test. Data are representative of three (A, F–I, and K–M) or four independent experiments (B–E and J). Source data are available for this figure: SourceData F6.

ester (Fluo-4 AM), a cell-permeable and sensitive Ca^{2+} indicator, in HEK293T cells following exposure to ATP. Consistent with previous reports (Blachier and Malaisse, 1988), exposure of cells to ATP resulted in a rapid increase in intracellular Ca^{2+} levels (Fig. 6 C). While cells overexpressing FNIP1 showed a higher peak of Ca^{2+} (F_t/F_0) transients compared with control cells in response to ATP stimulation (Fig. 6, C and D), FNIP1 overexpression resulted in significant decrease in the full duration at half maximum (FDHM) and time constant Tau of the Ca^{2+} transients (Fig. 6 E), indicating a faster cytosolic Ca^{2+} removal by SERCA2b in the presence of FNIP1. Taken together, these data suggest that FNIP1 binds to the ATP hydrolysis site of SERCA, and this leads to increased SERCA pump activity, thereby shaping intracellular Ca^{2+} dynamics.

Recently, FNIP1 was shown to regulate protein stability by modulating the chaperone function of Hsp90 (Sager et al., 2019; Sager et al., 2018; Woodford et al., 2016). We also sought to determine whether FNIP1 can also regulate SERCA2 protein stability. Interestingly, cycloheximide chase experiments in HEK293T cells revealed an increased stability of SERCA2b protein in cells overexpressing FNIP1 (Fig. 6 F). Moreover, SERCA2 protein levels were decreased in iWAT from FNIP1 AKO mice as compared with WT controls (Fig. 6 G). Together, these data suggest that FNIP1 also stabilizes SERCA2 protein. We next examined the SERCA ATPase activity in adipose tissue of FNIP1 AKO mice. As shown in Fig. 6 H, SERCA ATPase activity was markedly reduced in iWAT samples prepared from FNIP1 AKO mice compared with WT controls (Fig. 6 H). These in vivo results demonstrate an impaired SERCA activity in FNIP1 AKO adipose tissue, which is consistent with our in vitro observations that FNIP1 interacts with SERCA2b to preserve its activity. We also examined SERCA ATPase activity in homogenates of primary adipocytes and found decreased activity in FNIP1 KO adipocytes compared with WT controls (Fig. 6 I). Consistent with this finding, the Ca^{2+}-transporting activity of microsomes prepared from FNIP1 KO adipocytes was significantly lower compared with those isolated from WT control cells (Fig. 6 J). Moreover, we also monitored intracellular Ca^{2+} dynamics in FNIP1 KO adipocytes following exposure to ATP. As expected, FNIP1 ablation resulted in significant increase in the FDHM and time constant Tau of the Ca^{2+} transients (Fig. 6, K–M), indicating a slower cytosolic Ca^{2+} removal by SERCA in the absence of FNIP1. Taken together, these data suggest that loss of FNIP1 resulted in reduced SERCA Ca^{2+} pump activity, leading to enhanced intracellular Ca^{2+} signals.

Deletion of FNIP1 activates Ca^{2+}-dependent thermogenic program in white adipocytes

To further assess the role of FNIP1 in the control of intracellular Ca^{2+} homeostasis in adipocytes, we monitored the real-time intracellular Ca^{2+} changes in FNIP1 KO adipocytes upon NE stimulation using the Fluo-4 AM Ca^{2+} indicator. Consistent with reduced SERCA activity, the NE-induced increase in intracellular Ca^{2+} levels was greater in FNIP1 KO adipocytes than in WT control cells (Fig. 7, A–C). The FDHM and Tau of the Ca^{2+} transients triggered by NE were both increased in FNIP1 KO adipocytes, indicating an increased duration of Ca^{2+} transients in the cytosol in the absence of FNIP1 (Fig. 7 C). We also took advantage of the GCaMP6f reporter system and isolated primary adipocytes from iWAT of GCaMP6f/FNIP1 KO mice. Again, in response to NE stimulation, a more robust increase in GCaMP6f signals was observed in FNIP1 KO adipocytes compared with WT control cells (Fig. 7, D–F). Analysis of the GCaMP6f signals further confirmed the increased FDHM and Tau of the Ca^{2+} transients triggered by NE in FNIP1 KO adipocytes (Fig. 7 F). Together, these results suggest that deletion of FNIP1 in adipocytes resulted in impaired SERCA Ca^{2+} pump activity, leading to enhanced NE-elicited intracellular Ca^{2+} dynamics.

The enhanced intracellular Ca^{2+} dynamics were accompanied by increased cellular respiration capacity in FNIP1 KO adipocytes (Fig. 7 G). Measurement of oxygen consumption rate (OCR) using an extracellular flux analyzer revealed that FNIP1 KO adipocytes had an increased OCR in the presence of uncoupler carbonyl cyanide 4-(trifluoromethoxy)phenylhydrazone (FCCP), a sign of increased maximal mitochondrial respiratory capacity (Fig. 7 G). Importantly, depletion of intracellular Ca^{2+} by Ca^{2+} chelator BAPTA-AM inhibited the FNIP1 KO-mediated stimulatory effect (Fig. 7 H).

To further ascertain the role of FNIP1 in the control of white adipocyte thermogenic gene program and to determine whether Ca^{2+} signaling is involved in this mechanism, the effects of FSK and FNIP1 KO were assessed alone and together in the presence or absence of Ca^{2+} chelator BAPTA-AM. Interestingly, while *Ucp1* (20-fold) and *Ppargc1a* (8-fold) expression was activated by FSK, the combination of FSK and FNIP1 deficiency resulted in more activation of *Ucp1* (36-fold) and *Ppargc1a* (16-fold) gene expression in white adipocytes (Fig. 7 I). Importantly, this effect was largely abolished upon BAPTA-AM treatment (Fig. 7 I). β3-Adrenergic receptor agonist CL316,243 and FNIP1 deficiency also cooperated to increase expression of the *Ucp1* and *Ppargc1a* genes, an effect that was absent upon BAPTA-AM application (Fig. 7 J). Taken together, these results establish a key role of FNIP1 as a negative regulator of white adipocyte thermogenic remodeling and demonstrate the importance of intracellular Ca^{2+} in this mechanism.

Lack of adipocyte FNIP1 improves systemic glucose homeostasis and alleviates hepatic steatosis in obese mice

Browning of WAT is associated with a healthy metabolic profile. We next challenged FNIP1 AKO mice with a high-fat diet (HFD; 60% kcal from fat) for 3 mo. Interestingly, no difference was observed in body weight between the HFD-fed FNIP1 AKO mice and HFD-fed WT controls (Figs. 8 A and S4 A). HFD-fed FNIP1 AKO mice also showed no difference in food intake or locomotor activity but did have slight increases in oxygen consumption (VO_2) and carbon dioxide production (VCO_2; Fig. 8, A–C; and Fig. S4, B and C), implying the enhanced mitochondrial respiration in the adipose tissue. We then determined systemic glucose homeostasis in WT and FNIP1 AKO mice following HFD feeding. Glucose tolerance test (GTT) demonstrated that FNIP1 AKO mice were more tolerant to glucose challenge compared with the littermate controls after 12 wk of HFD feeding, even when there was no difference in body weight between the two groups (Fig. 8 D). Similarly, insulin tolerance test (ITT) showed that

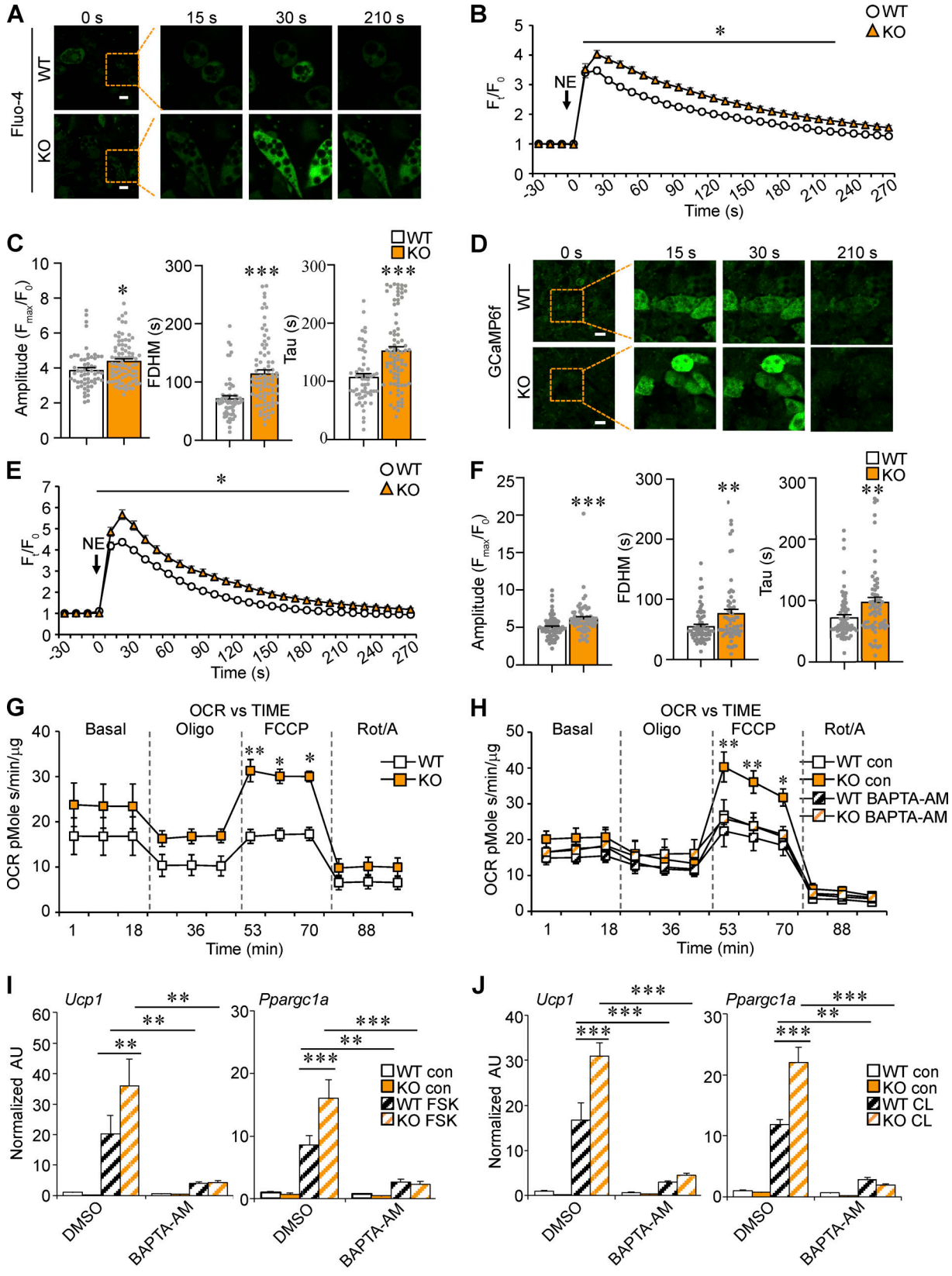

Figure 7. **Deletion of FNIP1 activates Ca^{2+}-dependent thermogenic program in white adipocytes. (A–C)** Ca^{2+} transients in differentiated white adipocyte isolated from iWAT of male WT and FNIP1 KO mice. Ca^{2+} dynamics were monitored using Fluo-4 AM in cells following exposure to 1 µM NE. *n* = 58–81 cells per group from five independent experiments. **(A)** Representative time-lapse images of indicated adipocytes at different time intervals after NE stimulation. Scale bars: 20 µm. **(B)** Quantitative analysis of the Fluo-4 AM fluorescence intensity (F_t/F_0). **(C)** Quantitation of amplitude, FDHM, and time constant Tau of Ca^{2+} transients. **(D–F)** Ca^{2+} transients in differentiated white adipocyte isolated from iWAT of male GCaMP6f transgenic and GCaMP6f; FNIP1 KO mice. *n* = 64–70

cells per group from five independent experiments. **(D)** Representative time-lapse images of indicated adipocytes at different time intervals after NE stimulation. Scale bars: 50 µm. **(E)** Quantitative analysis of the GCaMP6f fluorescence intensity (F_t/F_0). **(F)** Quantitation of amplitude, FDHM, and time constant Tau of Ca^{2+} transients. **(G and H)** OCRs in differentiated white adipocyte isolated from iWAT of male WT and FNIP1 KO mice. Basal OCR was first measured, followed by administration of 2 µM oligomycin (to inhibit ATP synthase), uncoupler FCCP (2 µM), or rotenone/antimycin (Rot/A; 1 µM) as indicted. *n* = 3 independent experiments done with 5–7 biological replicates. **(H)** Cells were pre-incubated with 10 µM BAPTA-AM for 2 h as indicated in the key. **(I and J)** Gene expression (qRT-PCR) in differentiated white adipocyte isolated from iWAT of male WT and FNIP1 KO mice. Cells were treated for 4 h with DMSO (vehicle), 10 µM FSK, 20 µM CL, 10 µM BAPTA-AM, FSK + BAPTA-AM, or CL + BAPTA-AM as indicated in the key. *n* = 3 independent experiments. Values represent mean ± SEM. *, P < 0.05; **, P < 0.01; ***, P < 0.001. P value was determined using two-tailed unpaired Student's *t*-test (B, C, E, and F), one-way ANOVA and Fisher's LSD post-hoc test (I and J), or two-way ANOVA and Bonferroni post-hoc test (G and H). Data are representative of at least three independent experiments (A–J).

HFD-fed FNIP1 AKO mice were more sensitive to insulin stimulation compared with HFD-fed WT controls (Figs. 8 E and S4 D). Moreover, insulin action, as indicated by insulin-stimulated AKT phosphorylation, in both adipose and skeletal muscle was enhanced in HFD-fed FNIP1 AKO mice (Fig. 8, F–G).

We next examined lipid metabolism in adipose tissue. The iWAT mass was reduced in the FNIP1 AKO mice relative to their WT controls at the end of HFD studies (Fig. 8 H). Histological analysis also showed smaller adipocytes in iWAT of HFD-fed FNIP1 AKO mice (Fig. 8 I). Moreover, mitochondrial respiration rates were significantly higher in iWAT of HFD-fed FNIP1 AKO mice compared with WT controls (Fig. 8 J). This primary alteration in adipose tissue was also associated with improved hepatic steatosis in HFD-fed FNIP1 AKO mice. Liver mass was lower in FNIP1 AKO mice (Fig. 8 K), and Oil-Red-O and H&E staining of histological sections provided further evidence of significantly reduced liver fat deposition in HFD-fed FNIP1 AKO mice (Fig. 8 L). Biochemical measurements confirmed a decrease in TG levels in HFD-fed FNIP1 AKO livers (Fig. 8 M). The protein levels of fatty acid synthase (FASN) were also decreased in the liver of HFD-fed FNIP1 AKO mice relative to WT controls (Fig. 8 N). Collectively, all these results suggest a healthier metabolic profile in FNIP1 AKO mice than in WT controls when fed an HFD. Taken together, these results demonstrate that deletion of FNIP1 in adipocytes results in browning of WAT with strong effects on whole-body glucose homeostasis and hepatic steatosis.

Discussion

The benefits of beige adipocytes on metabolic health make it a desirable therapeutic strategy to promote beige adipocyte thermogenic remodeling to treat obesity and metabolic diseases. Delineation of the molecular mechanisms involved in WAT browning is thus of particular interest. In this study, we uncovered a crucial role for FNIP1 in controlling WAT browning that governs systemic glucose homeostasis (Fig. 9). Mechanistically, FNIP1 binds to the ATP hydrolysis site of SERCA, and this leads to increased SERCA Ca^{2+} pump activity, thereby dampening Ca^{2+}-dependent thermogenic program. Importantly, adipocyte-specific ablation of FNIP1 led to a broad thermogenic remodeling of WAT and protected the mice from HFD-induced glucose intolerance, insulin resistance, and liver steatosis. Taken together, our study establishes a pivotal role of FNIP1 as a negative regulator of beige adipocyte thermogenesis, functionally linking intracellular Ca^{2+} dynamics to WAT browning.

FNIP1 protein has been implicated in regulating cellular metabolism in both humans and mice, and it is best known to exert its regulatory actions on both AMPK and mTOR signaling (Baba et al., 2006; Petit et al., 2013; Saettini et al., 2021; Siggs et al., 2016; Tsun et al., 2013; Xiao et al., 2021). Herein, we demonstrated that FNIP1 is a crucial negative regulator of adipocytes thermogenesis and systemic glucose metabolism. Thus, our study has expanded the role of FNIP1 to include pivotal WAT browning physiological functions. In addition, FNIP1 interacting partner FLCN has also been shown to act through AMPK or mTOR signaling to regulate adipocyte thermogenic reprogramming (Wada et al., 2016; Yan et al., 2016). Interestingly, however, our results suggest that loss of adipocyte FNIP1 promotes WAT thermogenic remodeling without affecting AMPK or mTOR signaling. The identification of FNIP1 as a regulator of cellular Ca^{2+} dynamics not only provides new mechanistic insight into how FNIP1 regulates cellular metabolism but also suggests broader functions of FNIP1 in directing more context-specific biological processes beyond AMPK or mTOR signaling. Notably, a small mutant form of FNIP1 protein could be theoretically expressed in the FNIP1-deficient line used in this study. Future studies will be necessary to investigate whether this smaller FNIP1 mutant protein retains partial function.

The molecular regulatory pathways that drive the formation of beige adipocytes have been well described (Cohen and Kajimura, 2021; Harms and Seale, 2013; Kajimura et al., 2015). However, the counterbalancing negative regulatory mechanisms remain less clear. Here, we show that FNIP1 acts as an endogenous "brake" to inhibit beige adipocyte thermogenesis. Importantly, the thermogenic remodeling in FNIP1 AKO mice exerts profound effects on whole-body metabolism when mice are fed an HFD, leading to improved systemic glucose homeostasis and hepatic steatosis. This is consistent with previous reports that browning of WAT is a key contributor to metabolic health (Bartelt and Heeren, 2014; Cohen and Kajimura, 2021; Harms and Seale, 2013; Kajimura et al., 2015; Kusminski et al., 2016). One of the intriguing findings from our study is that the marked brown remodeling of WAT in the FNIP1 AKO mice can occur without change to body weight, despite no difference in food intake. The reason for this difference is not clear. This could reflect a combined regulatory effect. Indeed, evidence is emerging that regulatory mechanisms, including but not limited to the efficiency in dietary nutrients absorption, have been shown to affect individual vulnerability to obesity. It is tempting to speculate that such mechanisms are active in FNIP1 AKO mice such that the bodyweight is not changed in FNIP1 AKO mice.

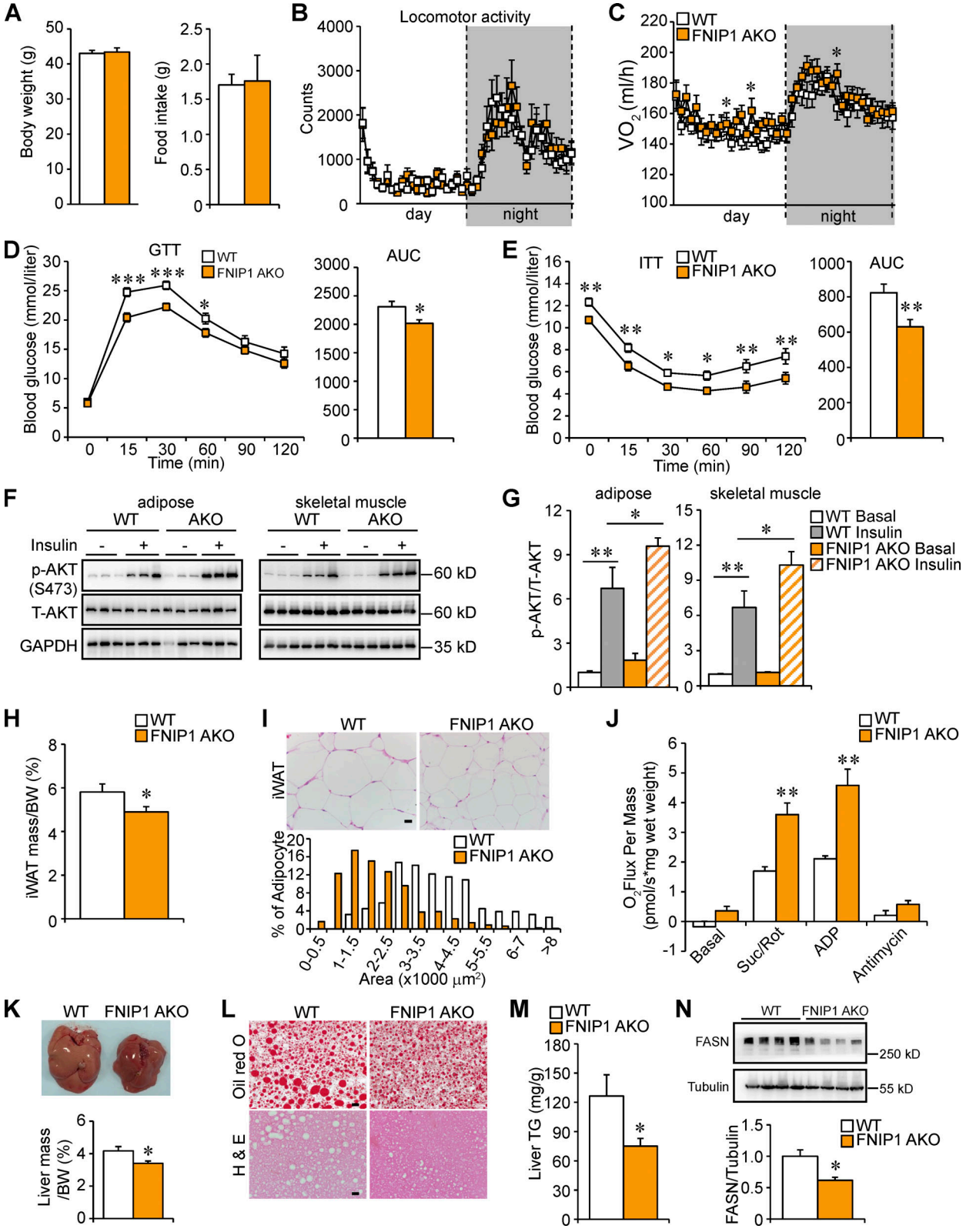

Figure 8. **Lack of adipocyte FNIP1 improves systemic glucose homeostasis and alleviates hepatic steatosis in obese mice. (A)** Left: Body weight of indicated male mice fed on HFD for 16 wk. *n* = 18–21 mice per group. Right: Food consumption per day. *n* = 6–12 mice per group. **(B)** Locomotor activity over 12-h light/dark cycle. *n* = 12–13 mice per group. **(C)** Oxygen consumption per hour during the light/dark cycle. *n* = 14–15 mice per group. **(D)** Left: GTT. Prior to studies, mice were fasted overnight. Right: Area under the curve for GTT is shown. *n* = 13–16 mice per group. **(E)** Left: ITT. Prior to studies, mice were fasted for 4 h. Right: Area under the curve for ITT is shown. *n* = 13–16 mice per group. **(F)** Representative Western blot analysis of Akt (S473) phosphorylation status relative to total AKT (T-AKT) in adipose and skeletal muscle 30 min after an intraperitoneal injection of insulin (2 U/kg) or saline in indicated male mice fed an

HFD. All mice were fasted overnight before insulin or saline injection. **(G)** Quantification of p-AKT (S473)/T-AKT signal ratios. *n* = 3–4 mice per group. **(H)** Weights of iWAT normalized to body weight. *n* = 10–11 mice per group. **(I)** Top: Representative H&E staining of iWAT from indicated male mice fed an HFD. Scale bar: 20 µm. (Bottom) Cross-sectional areas of iWAT were measured by ImageJ. *n* = 5–7 mice per group. **(J)** Mitochondrial respiration rates were determined from the iWAT of the indicated male mice fed on HFD using succinate as substrate. *n* = 5–6 mice per group. **(K)** Top: Picture of liver from indicated male mice fed an HFD. Bottom: Weights of liver mass normalized to body weight. *n* = 10–11 mice per group. **(L)** Oil-Red (top) and H&E stain (bottom) of liver from HFD-fed male FNIP1 AKO mice and WT controls. Scale bar: 20 µm. *n* = 6–9 mice per group. **(M)** Liver triglyceride levels from HFD-fed male FNIP1 AKO mice and WT controls. *n* = 6–10 mice per group. **(N)** Top: Representative Western blot analysis of liver lysates for HFD-fed male mice of the indicated genotypes. Bottom: Quantification of the FASN/tubulin signal ratios. *n* = 4 mice per group. Values represent mean ± SEM. *, P < 0.05; **, P < 0.01; ***, P < 0.001. P value was determined using two-tailed unpaired Student's *t*-test (A, H–K, M, and N), one-way ANOVA and Fisher's LSD post-hoc test (G), or two-way ANOVA and Fisher's LSD post-hoc test (B–E). Data are representative of two independent experiments (A–N). Source data are available for this figure: SourceData F8.

Ca^{2+} signals are fundamental to numerous cellular processes in virtually all eukaryotic cells (Arruda and Hotamisligil, 2015; Berridge et al., 2000; Giorgi et al., 2018; Raffaello et al., 2016). However, the role of Ca^{2+} signaling in the browning of WAT remains largely unexplored, in part, because of a limited understanding of the regulatory mechanism that controls intracellular Ca^{2+} dynamics in adipocytes. In this study, we demonstrated that FNIP1 acts as a positive regulator of ER Ca^{2+}-ATPase SERCA in adipocytes. In FNIP1 KO adipocytes, the reuptake of cytosolic Ca^{2+} into the ER lumen mediated by SERCA is reduced, resulting in elevated Ca^{2+} levels and increased duration of Ca^{2+} transients in the cytosol upon external stimuli. More importantly, we show that functionally, loss of FNIP1 triggers more robust thermogenic reprogramming in white adipocytes. Thus, we have identified a previously unrecognized intracellular Ca^{2+} dynamics regulatory pathway involved in WAT browning.

Notably, our results suggest that FNIP1 can also regulate SERCA2 protein stability, and this likely adds another regulatory layer to modulate the SERCA pump. Evidence has emerged that FNIP1 could act as a co-chaperone that regulates the chaperone function of Hsp90 (Sager et al., 2019; Sager et al., 2018; Woodford et al., 2016). Previous studies have revealed that the C-terminal region of FNIP1 binds to Hsp90, while the N-terminal region of FNIP1 interacts with Hsp90 clients (Woodford et al., 2016). Indeed, we found that the N-terminal region of FNIP1 binds to the ATP hydrolysis site of the SERCA pump. More interestingly, a public database has suggested that SERCA2 may be a client of Hsp90 (https://www.picard.ch/downloads/Hsp90interactors.pdf). It would seem likely that FNIP1 functions as a co-chaperone of Hsp90 that regulates chaperoning of SERCA2. Future studies will be necessary to further delineate this interesting FNIP1/Hsp90/SERCA2 mechanism.

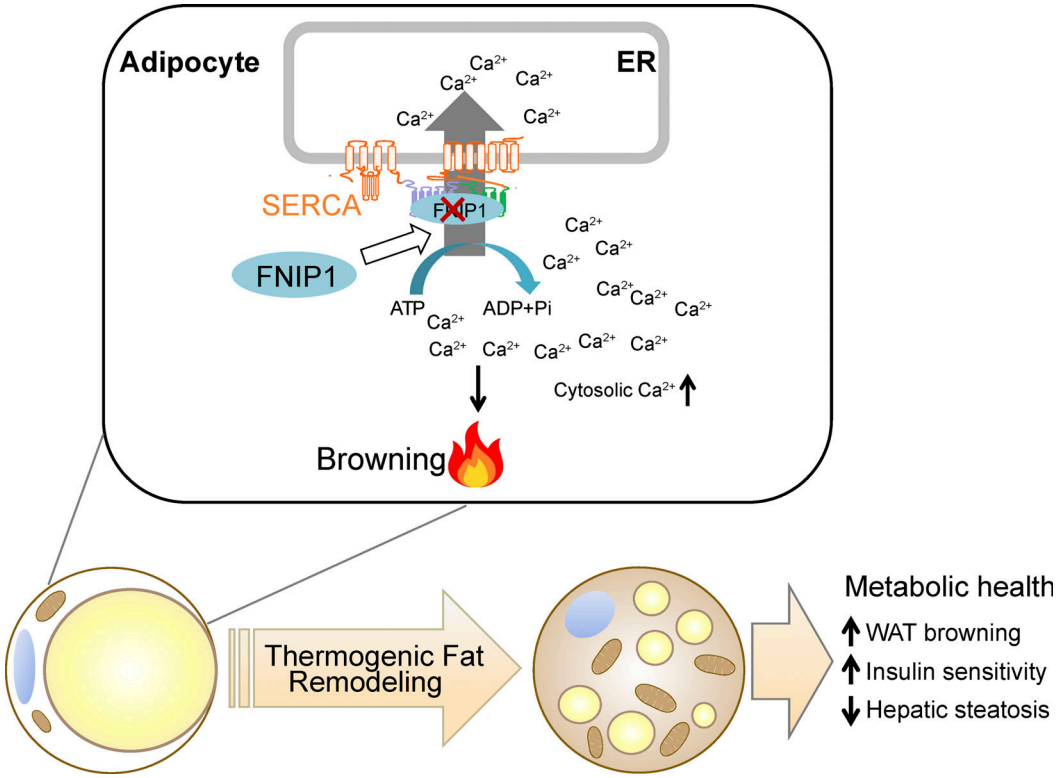

Figure 9. **Model of FNIP1 in the control of intracellular Ca^{2+} homeostasis and WAT browning.** The schematic depicts a proposed model for the FNIP1 regulatory mechanism that controls the intracellular Ca^{2+} dynamics and browning of WAT.

Although our results provide significant evidence that adipocyte FNIP1 shapes intracellular Ca^{2+} dynamics and regulates WAT browning, the precise mechanisms involved in the activation of the thermogenic program via enhanced intracellular Ca^{2+} signals were not fully determined in this study. Ca^{2+}-dependent kinases have been shown to activate the transcriptional programming of mitochondrial lipid metabolism via PGC-1α (Maurya et al., 2018; Maus et al., 2017), thereby suggesting one possible mechanism. In addition, mitochondria function is also directly regulated by Ca^{2+} (Ding et al., 2018; Raffaello et al., 2016), and it is also possible that the increased Ca^{2+} flux into the mitochondria leads to activation of mitochondrial oxidative metabolism in FNIP1 KO adipocytes. In the same lines, it has been shown that reductions in SERCA activity due to Seipin mutant also lead to elevated cytosolic Ca^{2+} levels with enhanced mitochondrial function and fat utilization in Drosophila (Bi et al., 2014; Ding et al., 2018). Notably, a recent study has shown that enhanced Ca^{2+} cycling in beige fat via the SERCA2-RyR pathway can promote a UCP1-independent thermogenesis (Ikeda et al., 2017). It warrants further investigation if FNIP1 also contributes to the regulation of beige adipocytes Ca^{2+} cycling.

In summary, we have revealed a crucial role of FNIP1 as a negative regulator of beige adipocyte thermogenesis and unravel an intriguing functional link between intracellular Ca^{2+} dynamics and WAT browning. Given the remarkable benefits of beige adipocytes on metabolic health and its demonstrated presence in adult humans, the regulatory network described here provides new therapeutic opportunities for enhancing WAT browning to combat obesity and metabolic diseases.

Materials and methods

Animal studies

All animal studies were conducted in strict accordance with the institutional guidelines for the humane treatment of animals and were approved by the Institutional Animal Care and Use Committee at the Model Animal Research Center of Nanjing University. WT C57BL/6J mice were from GemPharmatech Co., Ltd. *Fnip1*$^{f/f}$ mice were generated by the transgenic mouse facility at the Model Animal Research Center of Nanjing University. Briefly, the Cas9 system targeting the exon 6 of the C57BL/6J mice *Fnip1* gene was applied. The loxP sites were introduced upstream and downstream of exon 6 (92 bp) of the *Fnip1* gene by homologous recombination. Deletion of the exon 6 sequence of *Fnip1* resulted in a frame-shift and premature termination codon in exon 7 (Baba et al., 2012). The PCR primers for genotyping are listed in Table S1. To generate mice with an adipose tissue–specific disruption of the *Fnip1* allele (referred to as FNIP1 AKO), *Fnip1*$^{f/f}$ mice were crossed with mice expressing Cre recombinase under control of the adiponectin (*Adipoq*) promotor (stock no. 028020; The Jackson Laboratory). Generation of FNIP1 KO and muscle-specific *Fnip1* overexpression (*Fnip1*^{Tg}) mice have been described previously in detail (Xiao et al., 2021). The RCL-GCaMP6f mice (Ai95D; stock no. 024105; The Jackson Laboratory) were crossed with mice expressing Cre recombinase under control of the EIIa promoter (stock no. 003724; The Jackson Laboratory) to achieve expression of GCaMP6f, and these mice were then crossed with FNIP1 KO mice to obtain GCaMP6f/FNIP1 KO mice. Of note, although the majority of the phenotypic and molecular endpoints were collected in male mice, several readouts, including adrenergic thermogenesis and cold tolerance compared with littermate controls, were similar in male compared with female for FNIP1 AKO lines. Mice were allowed ad libitum access to standard laboratory rodent chow or HFD (60% of calories from fat; Research Diets no. D12492) as indicated. Cohorts of ≥3 mice per genotype were analyzed for all in vivo phenotypic studies, which were repeated at least two independent times. Mice were randomly assigned to various analyses. Littermate controls were used in all cases. Investigators involved in the immunofluorescence imaging, RNA-seq, and histological analysis were blinded. Investigators performing animal handling, sampling, and raw data collection were not blinded.

Primary adipocyte culture

Primary adipocytes were isolated and cultured as previously described (Arcinas et al., 2019; Fu et al., 2018). Briefly, ∼10-d-old mice were sacrificed. iWATs were harvested and digested with collagenase I (0.2%). Primary adipocytes were filtered through 70 μm and then collected by centrifugation at 1,300 *g* for 5 min. Primary adipocytes were cultured to confluence in high DMEM with 10% fetal calf serum (Gibco) and induced to differentiation for 2 or 3 days with high DMEM containing 10% FBS, insulin 850 nM (Sigma-Aldrich), dexamethasone 0.5 μM (Sigma-Aldrich), isobutyl methylxanthine 250 μM (Sigma-Aldrich), and Rosiglitazone 1 μM (Sigma-Aldrich). The induction medium was replaced with high DMEM containing 10% FBS and 160 nM insulin for another 2 or 3 d. Then cells were incubated in high DMEM with 10% FBS for 1–2 d. Differentiated white adipocytes were treated with DMSO (Sigma-Aldrich), TG (Sigma-Aldrich), CL (Sigma-Aldrich), or FSK (Sigma-Aldrich) for 4 h before harvest. For BAPTA-AM (Sigma-Aldrich) studies, cells were pre-incubated with BAPTA-AM for 2 h before CL or FSK treatments.

Cell transfection and immunoprecipitation

pEGFP-N1-*FNIP1* was from Addgene (Plasmid # 49175). The flag-tagged full-length *Fnip1* and *Fnip1* deletion variants were generated by PCR amplification from cDNA of mouse *Fnip1*, followed by cloning into the pcDNA5-Flag vector. The HA-tagged full-length *ATP2A2* and *ATP2A2* deletion variants were generated by PCR amplification from cDNA of human *ATP2A2*, followed by cloning into the pcDNA5-HA vector. The PCR primers for cloning are listed in Table S1. All constructs were confirmed by DNA sequencing. HEK293T cells, human embryonic kidney cell line, were obtained from the American Type Culture Collection and were cultured at 37°C and 5% CO_2 in DMEM supplemented with 10% FBS, 1,000 U/ml penicillin, and 100 mg/ml streptomycin. Transient transfections in HEK293T cells were performed using PEI transfection reagent (Polysciences) following the manufacturer's protocol. Whole lysate from HEK293T cells 48 h posttransfection was used for co-IP studies. HEK293T cells or adipose tissues were collected in lysis buffer (50 mM Tris, pH 7.5, 150 mM NaCl, 2 mM EDTA, 1.5% NP40, 1× Complete [Roche], and 1 mM PMSF). 1 μg of M2 anti-FLAG (Sigma-Aldrich),

anti-HA (Sigma-Aldrich), anti-FNIP1, or control IgG antibodies were incubated with extract and protein G–conjugated agarose beads. The immunoprecipitated proteins were analyzed by immunoblotting.

Ca^{2+} imaging in vitro and in vivo

In vitro Ca^{2+} imaging was performed as described previously (Chen et al., 2017). Briefly, primary adipocytes were seeded onto Rat Tail collagen–coated glass bottom dish (cat. no. 801001; Nest Biotechnology Co., Ltd.). Cells were loaded with 5 μM Fluo-4 AM (Thermo Fisher Scientific) for 30 min per manufacturer's protocol (F14201; Thermo Fisher Scientific) and imaged in HBSS with 1 mM Mg^{2+}, 1 mM Ca^{2+}, and 20 mM glucose. Images were acquired every 1 s using a Zeiss LSM880 confocal microscope. The following filter Spectra was used: excitation 470/40, dichroic FT495, and emission 525/50. Fluo-4 AM–labeled adipocytes were kept in HBSS solution for 30 s and then stimulated with 1 μM NE. Total recording time was 300 s. Imaging data were processed using the Zeiss software. Fluo-4 intensity was quantified within a region of interest for each cell and expressed as the relative change in fluorescence F_t/F_0, where F_0 is the fluorescence level at the start of the experiment and F_t is the instant Fluo-4 intensity over the 300 s imaging period. F_{max} (peak intensity) is the highest Fluo-4 intensity. The decay time (Tau) was measured from the peak of Ca^{2+} transients to 63% from the peak to the basal level in the fading phase. These quantifications were performed in a blinded manner with Zeiss software. For movies, the image sequences were saved as movies by Zeiss LSM880 (Applied Precision), and the aggregates move 30 times faster than in real time.

Two-photon microscopy imaging analyses were conducted to monitor Ca^{2+} activity in adipose tissue in vivo using the GCaMP6f transgenic mice. Briefly, in vivo imaging was performed by placing the mouse iWAT tissue underneath an Olympus FVMPE-RS two-photon upright microscope (Olympus). Ca^{2+} signal was obtained by using a fluorescent filter (Excitation 410–455 nm, Dichroic FT475, and Emission 495–540 nm). A Titanium-Sapphire pulsed infrared laser (Olympus) was used to stimulate GFP at 900 nm. GCaMP6f mice were treated with NE (1 mg/kg) via intraperitoneal injection. Baseline images were also acquired before NE treatment. The same excitation laser power and acquisition settings were maintained in individual animals at different time points. Videos were obtained for 8 min at 512 × 512 resolution with a sampling interval of 10 s.

Microsome isolation and measurement of Ca^{2+} uptake

Microsomes enriched in ER membranes were isolated by differential centrifugation, as previously described (Bi et al., 2014; McKeel and Jarett, 1970). Briefly, adipose tissue or adipocytes were homogenized with a glass homogenizer on ice in homogenization buffer (10 mM Hepes, 0.3 M KCl, 0.5 M sucrose, 100 mM PMSF, 10× complete, pH 7.4). The homogenates were centrifuged at 8,000 *g* for 10 min at 4°C, then the supernatants were collected and centrifuged at 30,000 *g* for 2 h in a Beckman optima Max ultracentrifuge at 4°C. The final pellets (ER enriched microsomes) were collected and resuspended in homogenization buffer (10 mM Hepes, 0.1 M KCl, 0.25 M sucrose, 100 mM PMSF, 10× complete, pH 7.4) to determine protein content and Ca^{2+} uptake.

Measurement of Ca^{2+} transport from external media into the microsomal vesicles mediated via Ca^{2+}-ATPase (SERCA pump) was measured using a Fura-2 (Sigma-Aldrich) based method, as described previously (Kargacin and Kargacin, 1994). Briefly, the isolated microsomes were incubated in assay buffer containing 100 mM KCl, 10 mM Hepes (pH 7.4), 10 mM oxalate, 5 mM $MgCl_2$, 10 μM ruthenium red, and 2 μM Fura-2 free acid. The reaction was initiated by addition of 5 mM ATP and 2 μM Ca^{2+}. Ca^{2+} uptake velocity was calculated from the Fura-2 fluorescence using the following equation, free $Ca^{2+} = K_d \times \beta \times (R - R_{min})/(R_{max} - R)$, total Ca^{2+} = free Ca^{2+} + total Fura-2 − $(K_d \times$ total Fura-2$)/(K_d +$ free $Ca^{2+})$ and velocity = (vol/wt) × $(-\Delta$total $Ca^{2+}/\Delta t)$, where R is the ratio of 510 nm emission fluorescence intensity excited at 340 and 380 nM; R_{max} and R_{min} were determined by addition of 10 mM Ca^{2+} or 25 mM EGTA in assay buffer, respectively. The dissociation constant (K_d) for Fura-2/Ca^{2+} was 200 nM; β is the ratio of fluorescence intensity of Ca^{2+} free and Ca^{2+} bound form of Fura-2 at 380 nM; vol is the volume of solution in the microplate; and wt is the amount of microsomal protein (in mg). The Δtotal $Ca^{2+}/\Delta t$ was analyzed using Clampfit 10.4 (Molecular Devices). The linear portion of the slope after addition of Ca^{2+} was used for calculation of Ca^{2+} uptake rates in microsomes.

Measurement of SERCA ATPase activity

The ATPase activity of SERCA2 was examined with an ATPase Activity Assay kit (MAK113; Sigma-Aldrich) according to the manufacturer's instructions using multifunctional microplate reader (BioTek Synergy H1). Briefly, adipose tissue samples (20 mg) or adipocytes (~1 × 10^6 cells) were homogenized on ice in with 200 μl of ice-cold assay buffer (40 mM Tris, 80 mM NaCl, 8 mM MgAc2, 1 mM EDTA, pH 7.5). The homogenates were centrifuged at 14,000 rpm for 10 min at 4°C to remove insoluble material. The reaction was performed in the absence or presence of 10 μM TG at 30°C for 30 min. The TG-sensitive Ca^{2+}-ATPase (SERCA2-ATPase) was calculated by subtracting TG insensitive Ca^{2+}-ATPase activity from total activity and normalized to SERCA protein content.

Cycloheximide (CHX) chase assay

The stability of SERCA2 protein was determined by CHX chase assays. HEK293T cells were transiently transfected with HA-SERCA2b, Flag-FNIP1, or control vector for 36 h. Cells were treated with 10 μM CHX (Sigma-Aldrich) for the indicated time and then collected and lysed by Western blotting.

Adipocyte Oil-Red-O staining

The differentiated adipocytes were assessed using a typical Oil-Red-O staining. Cells were washed with D-PBS and fixed with 4% paraformaldehyde for 60 min. Cells were rinsed twice with deionized water, followed by adding Oil-Red-O in 60% isopropanol for 20 min, and rinsed again. The cells were mounted on coverslips, visualized, and photographed using Olympus (IX73) under 10× and 20× magnification.

Oxygen consumption measurements

Cellular OCRs and extracellular acidification rates were measured using the XF24 analyzer (Seahorse Bioscience Inc.) per the manufacturer's protocol as described previously (Liu et al., 2016; Xiao et al., 2021). Basal OCR was first measured in XF Assay Media without sodium pyruvate, followed by administration of sodium pyruvate to a final concentration of 1 mM. Uncoupled respiration was evaluated following the addition of oligomycin (2 µM) to inhibit ATP synthase, by addition of the uncoupler FCCP (2 µM), and then followed by the addition of rotenone/antimycin (1 µM). Immediately after measurement, total protein levels were measured with the Micro BCA Protein Assay Kit (Thermo Scientific) for data correction.

Mitochondrial respiration studies

Mitochondrial respiration rates were measured in saponin-permeabilized adipose tissues with succinate/rotenone or pyruvate/malate as substrate, as described previously (Fu et al., 2018). In brief, ~20 mg of inguinal adipose tissues was dissected and permeabilized with 50 µg/ml saponin in BIOPS solution (7.23 mM K_2EGTA, 2.77 mM CaK_2EGTA, 20 mM imidazole, 20 mM taurine, 50 mM potassium 2-[N-morpholino]-ethanesulfonic acid, 0.5 mM dithiothreitol, 6.56 mM $MgCl_2$, 5.7 mM ATP, and 14.3 mM phosphocreatine, pH 7.1). Measurement of oxygen consumption in permeabilized adipose tissues was performed in buffer Z (105 mM potassium 2-[N-morpholino]-ethanesulfonic acid, 30 mM KCl, 10 mM KH_2PO4, 5 mM $MgCl_2$, 5 mg/ml BSA, 1 mM EGTA, pH 7.4) at 37°C and in the oxygen concentration range of 220–150 nmol O_2/ml in the respiration chambers of an Oxygraph 2K (Oroboros Inc.). Following measurement of basal, succinate (5 mM)/rotenone (10 µM), pyruvate (10 mM)/malate (5 mM), or propionyl-carnitine (40 µM)/malate (5 mM) respiration, maximal (ADP-stimulated) respiration was determined by exposing the mitochondria to 4 mM ADP. Uncoupled respiration was evaluated following addition of oligomycin (1 µg/ml) or antimycin (1.5 µg/ml). Respiration rates were determined and normalized to tissue wet weight using Datlab 5 software (Oroboros Inc.), and the data were expressed as "pmol O_2 s-1 mg wet weight-1."

Transmission EM

Within a minute, adipose tissues were dissected and fixed in pre-fixed solution (2.0% EM grade glutaraldehyde and 2.5% formaldehyde), and immediately minced to 1 mm cubes. The adipose tissue samples were fixed in the same pre-fixed solution at room temperature for 30 min and then fixed overnight at 4°C. Samples were processed at Shandong Weiya Biotechnology Co., Ltd. for standard transmission EM processing and imaging.

Mitochondrial DNA analyses

Genomic/mitochondrial DNA was measured as described previously (Xiao et al., 2021). Mitochondrial DNA content was determined by SYBR Green analysis (Takara Bio). The levels of NADH dehydrogenase subunit 1 (mitochondrial DNA) were normalized to the levels of lipoprotein lipase (genomic DNA). The primer sequences are provided in Table S2.

RNA-seq studies

Transcriptomics analyses were performed using RNA-seq as described previously (Liu et al., 2019; Liu et al., 2020; Xiao et al., 2021). Total RNA was isolated from the inguinal fat of FNIP1 AKO and WT control mice using RNAiso Plus (Takara Bio). RNA-seq using Illumina HiSeq 4000 was performed by Beijing Novogene Bioinformatics Technology Co., Ltd. Two independent samples per group were analyzed. Paired-end and 150 nt reads were obtained from the same sequencing lane. Transcriptome sequencing libraries averaged 33 million paired reads per sample with 92.4% alignment to the mouse genome (UCSC mm10). The sequencing reads were then aligned to the UCSC mm10 genome assembly using TopHat 2.0.14 with the default parameters. Fragments per kb of exon per million mapped reads were calculated using Cufflinks 2.2.1. The criteria for a regulated gene were a fold change >1.5 (either direction) and a significant P value (<0.05) versus WT. For pathway analysis, the filtered data sets (Table S3) were uploaded into DAVID Bioinformatics Resources 6.8 to review the bio pathways using the Functional Categories database. The GO analysis was used to interpret data, and the regulated terms were ranked by P value. The RNA-seq data have been deposited in the NCBI Gene Expression Omnibus and are accessible through GEO series accession number GSE185067.

RNA analyses

Quantitative RT-PCR (qRT-PCR) was performed as described previously (Xiao et al., 2021). Briefly, total RNA was extracted from fat tissue or primary fat cell using RNAiso Plus (Takara Bio). The purified RNA samples were then reverse transcribed using the PrimeScript RT Reagent Kit with gDNA Eraser (Takara Bio). Real-time qRT-PCR was performed using the ABI Prism Step-One system with Reagent Kit from Takara Bio. Specific oligonucleotide primers for target gene sequences are listed in Table S2. Arbitrary units of target mRNA were corrected to the expression of *36b4*.

Antibodies and immunoblotting studies

Antibodies directed against NDUFB8 (14794-1-AP, 1:1,000; Proteintech), UQCRC2 (14742-1-AP, 1:1,000; Proteintech), COX4 (11242-1-AP, 1:1,000; Proteintech), ATP5A (14676-1-AP, 1:1,000; Proteintech), SDHA (14865-1-AP, 1:1,000; Proteintech), GAPDH (60004-1-Ig, 1:1,000; Proteintech), α-tubulin (bs1699, 1:5,000; Bioworld), FASN (#3180, 1:1,000; Cell Signaling Technology), p-AMPKα Thr172 (#2535, 1:1,000; Cell Signaling Technology), AMPKα (#5831, 1:1,000; Cell Signaling Technology), p-ACC Ser79 (#11818, 1:1,000; Cell Signaling Technology), ACC (#3676, 1:1,000; Cell Signaling Technology), p-mTOR Ser2448 (#5536, 1:1,000; Cell Signaling Technology), p-mTOR Ser2481 (#2974, 1:1,000; Cell Signaling Technology), mTOR (#2983, 1:1,000; Cell Signaling Technology), p-S6K (#9234, 1:1,000; Cell Signaling Technology), S6K (#2708, 1:1,000; Cell Signaling Technology), p-S6 (#4858, 1:1,000; Cell Signaling Technology), S6 (#2317, 1:1,000; Cell Signaling Technology), p-4EBP1 (#2855, 1:1,000; Cell Signaling Technology) and 4EBP1 (#9644, 1:1,000; Cell Signaling Technology), p-AKT Ser473 (#4060, 1:1,000; Cell Signaling Technology), AKT (#9272, 1:1,000; Cell Signaling Technology), SERCA2

(2A7-A1, 1:1,000; Thermo Fisher Scientific), Flag (F1804, 1:1,000; Sigma-Aldrich), HA (H9658, 1:1,000; Sigma-Aldrich), and FNIP1 were developed in the laboratory of Zhenji Gan with the help with Abcam (ab236547, 1:500; Abcam); Western blotting studies were performed as previously described (Fu et al., 2018; Xiao et al., 2021). Blots were normalized to α-tubulin. The total protein concentration was measured by BCA assay using Pierce BCA Assay Kit Protocol (Thermo Fisher Scientific). Equal total protein was loaded to each lane.

Metabolic measurements in vivo

Mice were housed individually in metabolic cages at a 12-h light and dark cycle with free access to food and water using the CLAMS (Columbus Instruments). Mice were acclimated in the metabolic cage for 1 d prior to recording according to the instructions of the manufacturer. Food, energy expenditure, physical activity, VO_2, and VCO_2 were assessed simultaneously. For adrenergic thermogenesis measurement, basal metabolic rates were monitored for subsequent 1 h until reaching steady-state, and then mice were injected intraperitoneally with CL (0.5 mg/kg; Sigma-Aldrich). The subsequent increase in metabolic rates was monitored for 6 h.

Cold exposure and core body temperature measurement

Mice were housed at 25°C for 3 d with free access to food and water. Mice were fasted for 12 h before cold-exposure experiments and were singly caged without food and exposed to a cold temperature at 4°C. The core body temperatures were measured using a rectal probe attached to a digital thermometer (Tianjin Jinming Instrument Co., Ltd.).

Glucose and insulin tolerance testing

Prior to studies, mice were fasted overnight (GTT) or for 4 h (ITT). For GTT studies, mice were injected with 1.5 g/kg of D-glucose. For ITT, mice received an intraperitoneal injection of human regular insulin (Sigma-Aldrich) at a dose of 0.75 U/kg bodyweight. Blood glucose levels were determined at 0, 15, 30, 60, 90, and 120 min after challenge using a OneTouch ultramini glucose meter (OneTouch). Area under the curve was defined as the difference between baseline glucose levels and the deflection caused by the glucose or insulin challenge. Total area under the curve was calculated using the trapezoidal rule.

Blood and tissue chemistry

After a 12-wk HFD regimen, mice were fasted overnight (16 h) beginning at 5 p.m. Blood samples were obtained. Liver tissue (50 mg) was homogenized and centrifuged supernatants were harvested. The TG levels were determined with the Free Glycerol Reagent (F6428; Sigma-Aldrich) using glycerol (G7793; Sigma-Aldrich) as standard for calculation.

Histological analyses

Livers of mice were embedded in Tissue-Tek OCT cryostat molds (Leica) and frozen at −80°C. 10-μm thick sections of livers were generated in a cryostat. Tissue sections were stained in 0.5% Oil-Red-O and H&E (Sigma-Aldrich) according to the standard protocol. Adipose tissues were fixed in 4% paraformaldehyde overnight at 4°C immediately after sacrifice, embedded in paraffin, and cut to 7-μm sections on slides using a Leica RM2016 microtome. The slides were stained with H&E. Quantification of cross-sectional area of the adipocyte was performed with NIH ImageJ software. At least 30 fields from random sections of each mouse sample were quantified. For UCP1 immunohistochemistry (IHC), adipose tissue sections were rehydrated and then boiled in 10 mM citric acid buffer, pH 6.0, at 95°C for antigen retrieval. Immunohistochemistry was performed using the UltraSensitiveTM SP (Rabbit) IHC Kit (Maxim) according to the manufacturer's instructions using rabbit UCP1 antibodies (ab10983; 1:500; Abcam). DAB Staining Kit (DAB-0031, Maxim) was used according to the manufacturer's instructions for development.

Statistical analysis

All mouse and cell studies were analyzed by Student's *t*-test when two groups were compared. One-way ANOVA or two-way ANOVA coupled with a Fisher's least significant difference (LSD) post-hoc test was used when more than two groups were compared. No statistical methods were used to predetermine sample sizes, and sample sizes (range from $n = 3$ to $n = 21$) are explicitly stated in the figure legends. All data points were used in statistical analyses. Data represents mean ± SEM with a statistically significant difference defined as a value of $P < 0.05$.

Online supplemental material

Fig. S1 shows the generation and characterization of mice with adipocyte-specific disruption of the *Fnip1* gene. Fig. S2 shows that loss of adipocyte FNIP1 leads to increased respiration and cold tolerance. Fig. S3 shows the identification of SERCA binding to FNIP1. Fig. S4 shows the metabolic characterization of male FNIP1 AKO mice fed on a high-fat diet. Table S1 lists genotyping and cloning primers. Table S2 lists RT-PCR primers. Table S3 lists up-regulated genes in FNIP1-AKO iWAT. Video 1 shows that real-time two-photon microscopy imaging of iWAT of GCaMP6f transgenic mice after 1 mg/kg NE stimulation. Video 2 shows that real-time imaging of white adipocytes isolated from iWAT of GCaMP6f transgenic mice after 1 μM NE stimulation.

Data availability

The adipose FNIP1 AKO RNA-seq data have been deposited to the NCBI Gene Expression Omnibus and are accessible through GEO series accession number GSE185067.

Acknowledgments

We wish to thank Dr. Li Qiang (Columbia University), Dr. Lei Sun (Duke-NUS Medical School), Dr. Yifu Qiu (Peking University), Dr. Yong Liu (Wuhan University), and Dr. Mengle Shao (Institut Pasteur of Shanghai Chinese Academy of Sciences) for thoughtful discussions.

This work was supported by grants from the National Natural Science Foundation of China (31922033, 91857105, 32071136, 32100922, and 32100942) to Z. Gan, T. Fu, and D. Xu; the Ministry of Science and Technology of China (National Key Research and Development Program of China 2018YFA0800700) to

Z. Gan; China Postdoctoral Science Foundation (2021M691524) to D. Xu; and Fundamental Research Funds for the Central Universities (021414380511) to Z. Gan.

Author contributions: Y. Yin, D. Xu, and Y. Mao designed and performed most of the experiments, analyzed the data, and wrote the manuscript. L. Xiao, Z. Sun, J. Liu, D. Zhou, Z. Xu, L. Liu, T. Fu, C. Ding, Q. Guo, W. Sun, Z. Zhou, L. Yang, Y. Jia, and X. Chen participated in the collection and analysis of the data. Z. Gan conceptualized, supervised, interpreted the experiments, and wrote the manuscript. All authors reviewed and contributed to the manuscript.

Disclosures: The authors declare that no competing interests exist.

Submitted: 14 December 2021
Revised: 14 February 2022
Accepted: 8 March 2022

References

Arcinas, C., W. Tan, W. Fang, T.P. Desai, D.C.S. Teh, U. Degirmenci, D. Xu, R. Foo, and L. Sun. 2019. Adipose circular RNAs exhibit dynamic regulation in obesity and functional role in adipogenesis. *Nat Metab.* 1: 688–703. https://doi.org/10.1038/s42255-019-0078-z

Arruda, A.P., and G.S. Hotamisligil. 2015. Calcium homeostasis and organelle function in the pathogenesis of obesity and diabetes. *Cell Metab.* 22: 381–397. https://doi.org/10.1016/j.cmet.2015.06.010

Baba, M., S.-B. Hong, N. Sharma, M.B. Warren, M.L. Nickerson, A. Iwamatsu, D. Esposito, W.K. Gillette, R.F. Hopkins, J.L. Hartley, et al. 2006. Folliculin encoded by the BHD gene interacts with a binding protein, FNIP1, and AMPK, and is involved in AMPK and mTOR signaling. *Proc. Natl. Acad. Sci. USA.* 103:15552–15557. https://doi.org/10.1073/pnas.0603781103

Baba, M., J.R. Keller, H.W. Sun, W. Resch, S. Kuchen, H.C. Suh, H. Hasumi, Y. Hasumi, K.R. Kieffer-Kwon, C.G. Gonzalez, et al. 2012. The folliculin-FNIP1 pathway deleted in human Birt-Hogg-Dube syndrome is required for murine B-cell development. *Blood.* 120:1254–1261. https://doi.org/10.1182/blood-2012-02-410407

Bal, N.C., S.K. Maurya, D.H. Sopariwala, S.K. Sahoo, S.C. Gupta, S.A. Shaikh, M. Pant, L.A. Rowland, S.A. Goonasekera, J.D. Molkentin, et al. 2012. Sarcolipin is a newly identified regulator of muscle-based thermogenesis in mammals. *Nat. Med.* 18:1575–1579. https://doi.org/10.1038/nm.2897

Bartelt, A., and J. Heeren. 2014. Adipose tissue browning and metabolic health. *Nat. Rev. Endocrinol.* 10:24–36. https://doi.org/10.1038/nrendo.2013.204

Berridge, M.J., P. Lipp, and M.D. Bootman. 2000. The versatility and universality of calcium signalling. *Nat. Rev. Mol. Cell Biol.* 1:11–21. https://doi.org/10.1038/35036035

Bi, J., W. Wang, Z. Liu, X. Huang, Q. Jiang, G. Liu, Y. Wang, and X. Huang. 2014. Seipin promotes adipose tissue fat storage through the ER Ca^{2+}-ATPase SERCA. *Cell Metab.* 19:861–871. https://doi.org/10.1016/j.cmet.2014.03.028

Blachier, F., and W.J. Malaisse. 1988. Effect of exogenous ATP upon inositol phosphate production, cationic fluxes and insulin release in pancreatic islet cells. *Biochim. Biophys. Acta.* 970:222–229. https://doi.org/10.1016/0167-4889(88)90182-6

Chen, Y., X. Zeng, X. Huang, S. Serag, C.J. Woolf, and B.M. Spiegelman. 2017. Crosstalk between KCNK3-mediated ion current and adrenergic signaling regulates adipose thermogenesis and obesity. *Cell.* 171: 836–848.e13

Chouchani, E.T., and S. Kajimura. 2019. Metabolic adaptation and maladaptation in adipose tissue. *Nat. Metab.* 1:189–200. https://doi.org/10.1038/s42255-018-0021-8

Cohen, P., and S. Kajimura. 2021. The cellular and functional complexity of thermogenic fat. *Nat. Rev. Mol. Cell Biol.* 22:393–409. https://doi.org/10.1038/s41580-021-00350-0

Cohen, P., J. Levy, J.D. Levy, Y. Zhang, A. Frontini, D. Kolodin, D.P. Kolodin, K. Svensson, K.J. Svensson, J. Lo, et al. 2014. Ablation of PRDM16 and beige adipose causes metabolic dysfunction and a subcutaneous to visceral fat switch. *Cell.* 156:304–316. https://doi.org/10.1016/j.cell.2013.12.021

Cypess, A.M., S. Lehman, G. Williams, I. Tal, D. Rodman, A.B. Goldfine, F.C. Kuo, E.L. Palmer, Y.H. Tseng, A. Doria, et al. 2009. Identification and importance of brown adipose tissue in adult humans. *N. Engl. J. Med.* 360:1509–1517. https://doi.org/10.1056/NEJMoa0810780

De Smedt, H., J.A. Eggermont, F. Wuytack, J.B. Parys, L. Van den Bosch, L. Missiaen, J. Verbis, and R. Casteels. 1991. Isoform switching of the sarco(endo)plasmic reticulum Ca^{2+} pump during differentiation of BC3H1 myoblasts. *J. Biol. Chem.* 266:7092–7095

Ding, L., X. Yang, H. Tian, J. Liang, F. Zhang, G. Wang, Y. Wang, M. Ding, G. Shui, and X. Huang. 2018. Seipin regulates lipid homeostasis by ensuring calcium-dependent mitochondrial metabolism. *EMBO J.* 37: e97572. https://doi.org/10.15252/embj.201797572

Fu, S., S.M. Watkins, and G.S. Hotamisligil. 2012. The role of endoplasmic reticulum in hepatic lipid homeostasis and stress signaling. *Cell Metab.* 15:623–634. https://doi.org/10.1016/j.cmet.2012.03.007

Fu, S., L. Yang, P. Li, O. Hofmann, L. Dicker, W. Hide, X. Lin, S.M. Watkins, A.R. Ivanov, and G.S. Hotamisligil. 2011. Aberrant lipid metabolism disrupts calcium homeostasis causing liver endoplasmic reticulum stress in obesity. *Nature.* 473:528–531. https://doi.org/10.1038/nature09968

Fu, T., Z. Xu, L. Liu, Q. Guo, H. Wu, X. Liang, D. Zhou, L. Xiao, L. Liu, Y. Liu, et al. 2018. Mitophagy directs muscle-adipose crosstalk to alleviate dietary obesity. *Cell Rep.* 23:1357–1372. https://doi.org/10.1016/j.celrep.2018.03.127

Giorgi, C., A. Danese, S. Missiroli, S. Patergnani, and P. Pinton. 2018. Calcium dynamics as a machine for decoding signals. *Trends Cell Biol.* 28:258–273. https://doi.org/10.1016/j.tcb.2018.01.002

Harms, M., and P. Seale. 2013. Brown and beige fat: Development, function and therapeutic potential. *Nat. Med.* 19:1252–1263. https://doi.org/10.1038/nm.3361

Ikeda, K., Q. Kang, T. Yoneshiro, J.P. Camporez, H. Maki, M. Homma, K. Shinoda, Y. Chen, X. Lu, P. Maretich, et al. 2017. UCP1-independent signaling involving SERCA2b-mediated calcium cycling regulates beige fat thermogenesis and systemic glucose homeostasis. *Nat. Med.* 23:1454–1465. https://doi.org/10.1038/nm.4429

Kajimura, S., B.M. Spiegelman, and P. Seale. 2015. Brown and Beige fat: Physiological roles beyond heat generation. *Cell Metab.* 22:546–559. https://doi.org/10.1016/j.cmet.2015.09.007

Kargacin, M.E., and G.J. Kargacin. 1994. Methods for determining cardiac sarcoplasmic reticulum Ca^{2+} pump kinetics from fura 2 measurements. *Am. J. Physiol.* 267:C1145–C1151. https://doi.org/10.1152/ajpcell.1994.267.4.C1145

Kusminski, C.M., P.E. Bickel, and P.E. Scherer. 2016. Targeting adipose tissue in the treatment of obesity-associated diabetes. *Nat. Rev. Drug Discov.* 15: 639–660. https://doi.org/10.1038/nrd.2016.75

Lee, S.C., R. Nuccitelli, and P.A. Pappone. 1993. Adrenergically activated Ca^{2+} increases in brown fat cells: Effects of Ca^{2+}, K^+, and K channel block. *Am. J. Physiol.* 264:C217–C228. https://doi.org/10.1152/ajpcell.1993.264.1.C217

Lidell, M.E., M.J. Betz, O. Dahlqvist Leinhard, M. Heglind, L. Elander, M. Slawik, T. Mussack, D. Nilsson, T. Romu, P. Nuutila, et al. 2013. Evidence for two types of brown adipose tissue in humans. *Nat. Med.* 19: 631–634. https://doi.org/10.4161/adip.26896

Liu, J., X. Liang, D. Zhou, L. Lai, L. Xiao, L. Liu, T. Fu, Y. Kong, Q. Zhou, R.B. Vega, et al. 2016. Coupling of mitochondrial function and skeletal muscle fiber type by a miR-499/Fnip1/AMPK circuit. *EMBO Mol. Med.* 8: 1212–1228. https://doi.org/10.15252/emmm.201606372

Liu, L., J. Cai, H. Wang, X. Liang, Q. Zhou, C. Ding, Y. Zhu, T. Fu, Q. Guo, Z. Xu, et al. 2019. Coupling of COPII vesicle trafficking to nutrient availability by the IRE1α-XBP1s axis. *Proc. Natl. Acad. Sci. USA.* 116:11776–11785. https://doi.org/10.1073/pnas.1814480116

Liu, L., C. Ding, T. Fu, Z. Feng, J.E. Lee, L. Xiao, Z. Xu, Y. Yin, Q. Guo, Z. Sun, et al. 2020. Histone methyltransferase MLL4 controls myofiber identity and muscle performance through MEF2 interaction. *J. Clin. Investig.* 130: 4710–4725. https://doi.org/10.1172/JCI136155

Locke, A.E., B. Kahali, S.I. Berndt, A.E. Justice, T.H. Pers, R. Felix, C. Powell, S. Vedantam, M.L. Buchkovich, J. Yang, et al. 2015. Genetic studies of body mass index yield new insights for obesity biology. *Nature.* 518:197–206. https://doi.org/10.1038/nature14177

Manford, A.G., E.L. Mena, K.Y. Shih, C.L. Gee, R. McMinimy, B. Martinez-Gonzalez, R. Sherriff, B. Lew, M. Zoltek, F. Rodriguez-Perez, et al. 2021. Structural basis and regulation of the reductive stress response. *Cell.* 184:5375–5390.e16. https://doi.org/10.1016/j.cell.2021.09.002

Manford, A.G., F. Rodriguez-Perez, K.Y. Shih, Z. Shi, C.A. Berdan, M. Choe, D.V. Titov, D.K. Nomura, and M. Rape. 2020. A cellular mechanism to detect and alleviate reductive stress. *Cell*. 183:46. https://doi.org/10.1016/j.cell.2020.08.034

Maurya, S.K., J.L. Herrera, S.K. Sahoo, F.C.G. Reis, R.B. Vega, D.P. Kelly, and M. Periasamy. 2018. Sarcolipin signaling promotes mitochondrial biogenesis and oxidative metabolism in skeletal muscle. *Cell Rep.* 24: 2919–2931. https://doi.org/10.1016/j.celrep.2018.08.036

Maus, M., M. Cuk, B. Patel, J. Lian, M. Ouimet, U. Kaufmann, J. Yang, R. Horvath, H.T. Hornig-Do, Z.M. Chrzanowska-Lightowlers, et al. 2017. Store-operated Ca^{2+} entry controls induction of lipolysis and the transcriptional reprogramming to lipid metabolism. *Cell Metab.* 25:698–712. https://doi.org/10.1016/j.cmet.2016.12.021

McKeel, D.W., and L. Jarett. 1970. Preparation and characterization of a plasma membrane fraction from isolated fat cells. *J. Cell Biol.* 44:417–432. https://doi.org/10.1083/jcb.44.2.417

Niehues, T., T.T. Oezguer, M. Bickes, R. Waldmann, J. Schoening, J. Braesen, C. Hagel, M. Ballmaier, J.-H. Klusmann, A. Niedermayer, et al. 2020. Mutations of the gene FNIP1 associated with a syndromic autosomal recessive immunodeficiency with cardiomyopathy and pre-excitation syndrome. *Eur. J. Immunol.* 50:1078–1080. https://doi.org/10.1002/eji.201948504

Periasamy, M., S.K. Maurya, S.K. Sahoo, S. Singh, S.K. Sahoo, F.C.G. Reis, and N.C. Bal. 2017. Role of SERCA pump in muscle thermogenesis and metabolism. *Compr. Physiol.* 7:879–890. https://doi.org/10.1002/cphy.c160030

Petit, C.S., A. Roczniak-Ferguson, and S.M. Ferguson. 2013. Recruitment of folliculin to lysosomes supports the amino acid-dependent activation of Rag GTPases. *J. Cell Biol.* 202:1107–1122. https://doi.org/10.1083/jcb.201307084

Prakriya, M., and R.S. Lewis. 2015. Store-operated calcium channels. *Physiol. Rev.* 95:1383–1436. https://doi.org/10.1152/physrev.00020.2014

Raffaello, A., C. Mammucari, G. Gherardi, and R. Rizzuto. 2016. Calcium at the center of cell signaling: Interplay between endoplasmic reticulum, mitochondria, and lysosomes. *Trends Biochem. Sci.* 41:1035–1049. https://doi.org/10.1016/j.tibs.2016.09.001

Reyes, N.L., G.B. Banks, M. Tsang, D. Margineantu, H. Gu, D. Djukovic, J. Chan, M. Torres, H.D. Liggitt, S.D. Hirenallur, et al. 2015. Fnip1 regulates skeletal muscle fiber type specification, fatigue resistance, and susceptibility to muscular dystrophy. *Proc. Natl. Acad. Sci. USA*. 112: 424–429. https://doi.org/10.1073/pnas.1413021112

Saettini, F., C. Poli, J. Vengoechea, S. Bonanomi, J.C. Orellana, G. Fazio, F.H. Rodriguez III, L.P. Noguera, C. Booth, V. Jarur-Chamy, et al. 2021. Absent B cells, agammaglobulinemia, and hypertrophic cardiomyopathy in folliculin-interacting protein 1 deficiency. *Blood*. 137:493–499. https://doi.org/10.1182/blood.2020006441

Sager, R.A., M.R. Woodford, S.J. Backe, A.M. Makedon, A.J. Baker-Williams, B.T. DiGregorio, D.R. Loiselle, T.A. Haystead, N.E. Zachara, C. Prodromou, et al. 2019. Post-translational regulation of FNIP1 creates a rheostat for the molecular chaperone Hsp90. *Cell Rep.* 26:1344–1356.e5. https://doi.org/10.1016/j.celrep.2019.01.018

Sager, R.A., M.R. Woodford, and M. Mollapour. 2018. The mTOR independent function of Tsc1 and FNIPs. *Trends Biochem. Sci.* 43:935–937. https://doi.org/10.1016/j.tibs.2018.09.018

Seale, P., H.M. Conroe, J. Estall, S. Kajimura, A. Frontini, J. Ishibashi, P. Cohen, S. Cinti, and B.M. Spiegelman. 2011. Prdm16 determines the thermogenic program of subcutaneous white adipose tissue in mice. *J. Clin. Investig.* 121:96–105. https://doi.org/10.1172/JCI44271

Shinoda, K., I.H.N. Luijten, Y. Hasegawa, H. Hong, S.B. Sonne, M. Kim, R. Xue, M. Chondronikola, A.M. Cypess, Y.H. Tseng, et al. 2015. Genetic and functional characterization of clonally derived adult human brown adipocytes. *Nat. Med.* 21:389–394. https://doi.org/10.1038/nm.3819

Siggs, O.M., A. Stockenhuber, M. Deobagkar-Lele, K.R. Bull, T.L. Crockford, B.L. Kingston, G. Crawford, C. Anzilotti, V. Steeples, S. Ghaffari, et al. 2016. Mutation of Fnip1 is associated with B-cell deficiency, cardiomyopathy, and elevated AMPK activity. *Proc. Natl. Acad. Sci. USA*. 113: E3706–E3715. https://doi.org/10.1073/pnas.1607592113

Tsun, Z.Y., L. Bar-Peled, L. Chantranupong, R. Zoncu, T. Wang, C. Kim, E. Spooner, and D.M. Sabatini. 2013. The folliculin tumor suppressor is a GAP for the RagC/D GTPases that signal amino acid levels to mTORC1. *Mol. Cell*. 52:495–505. https://doi.org/10.1016/j.molcel.2013.09.016

Verkerke, A.R.P., P.J. Ferrara, C.T. Lin, J.M. Johnson, T.E. Ryan, J.A. Maschek, H. Eshima, C.W. Paran, B.T. Laing, P. Siripoksup, et al. 2019. Phospholipid methylation regulates muscle metabolic rate through Ca^{2+} transport efficiency. *Nat. Metabol.* 1:876–885. https://doi.org/10.1038/s42255-019-0111-2

Wada, S., M. Neinast, C. Jang, Y.H. Ibrahim, G. Lee, A. Babu, J. Li, A. Hoshino, G.C. Rowe, J. Rhee, et al. 2016. The tumor suppressor FLCN mediates an alternate mTOR pathway to regulate browning of adipose tissue. *Genes Dev.* 30:2551–2564. https://doi.org/10.1101/gad.287953.116

Woodford, M.R., D.M. Dunn, A.R. Blanden, D. Capriotti, D. Loiselle, C. Prodromou, B. Panaretou, P.F. Hughes, A. Smith, W. Ackerman, et al. 2016. The FNIP co-chaperones decelerate the Hsp90 chaperone cycle and enhance drug binding. *Nat. Commun.* 7:12037. https://doi.org/10.1038/ncomms12037

Wu, J., P. Boström, L.M. Sparks, L. Ye, J.H. Choi, A.H. Giang, M. Khandekar, K.A. Virtanen, P. Nuutila, G. Schaart, et al. 2012. Beige adipocytes are a distinct type of thermogenic fat cell in mouse and human. *Cell*. 150: 366–376. https://doi.org/10.1016/j.cell.2012.05.016

Xiao, L., J. Liu, Z. Sun, Y. Yin, Y. Mao, D. Xu, L. Liu, Z. Xu, Q. Guo, C. Ding, et al. 2021. AMPK-dependent and -independent coordination of mitochondrial function and muscle fiber type by FNIP1. *PLoS Genet.* 17: e1009488. https://doi.org/10.1371/journal.pgen.1009488

Yan, M., É.S. Audet-WalshManteghi, C.R. Dufour, B. Walker, M. Baba, J. St-Pierre, V. Giguère, A. Pause, and A Pause. 2016. Chronic AMPK activation via loss of FLCN induces functional beige adipose tissue through PGC-1α/ERRα. *Genes Dev.* 30:1034–1046. https://doi.org/10.1101/gad.281410.116

Supplemental material

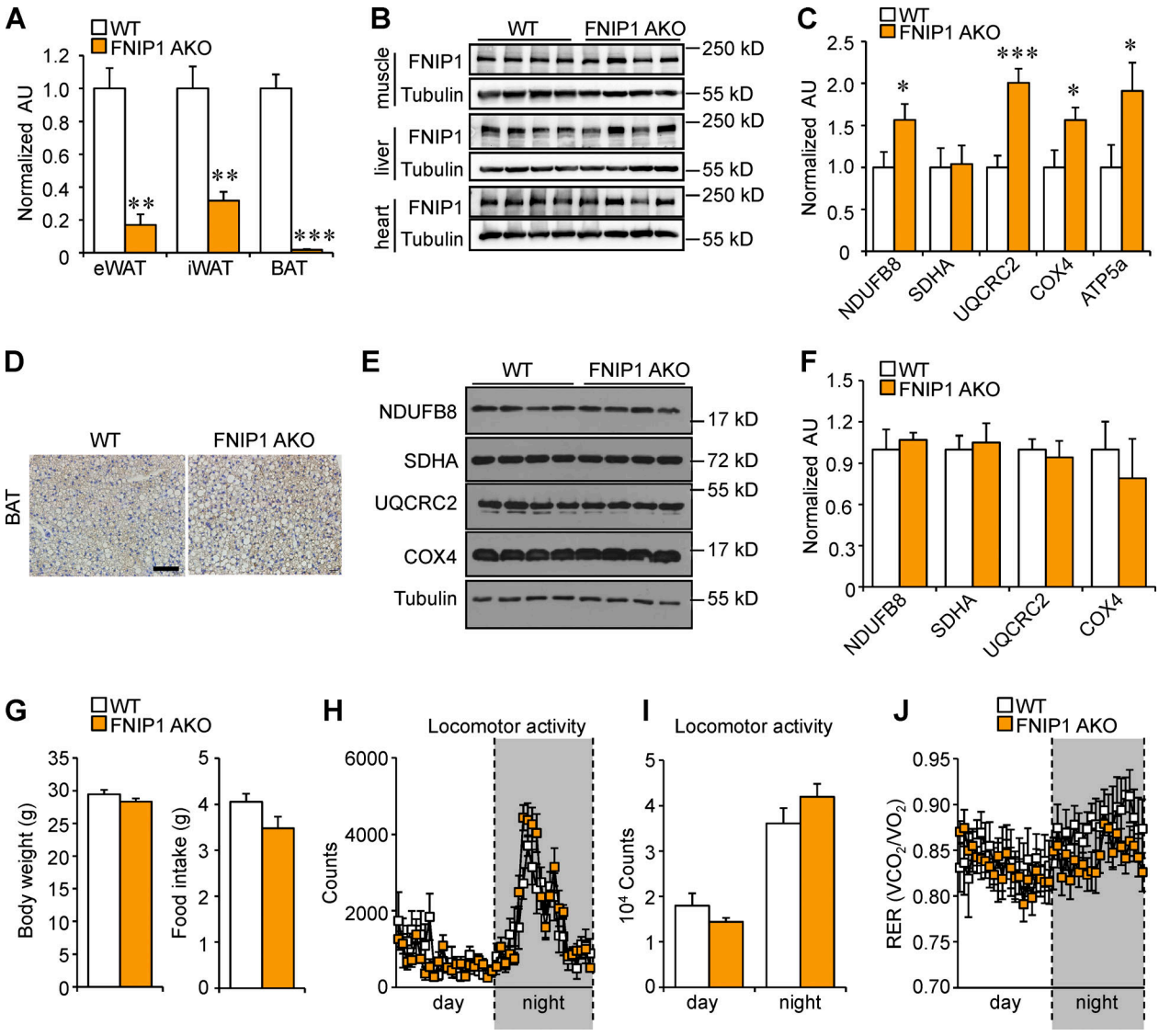

Figure S1. **Generation and characterization of mice with adipocyte-specific disruption of the *Fnip1* gene. (A)** qRT-PCR analysis of *Fnip1* expression in eWAT, iWAT, and BAT of male WT and FNIP1 AKO mice. *n* = 3–6 mice per group. **(B)** Representative Western blot analysis of FNIP1 protein expression in skeletal muscle, liver, and heart from indicated male mice. *n* = 8 mice per group. **(C)** Quantification of the NDUFB8/tubulin, SDHA/tubulin, UQCRC2/tubulin, COX4/tubulin and ATP5A/tubulin signal ratios in Fig. 1 I were normalized (= 1.0) to the WT control mice. *n* = 11–12 mice per group. **(D)** IHC staining with a UCP1-specific antibody in BAT sections of indicated male mice. Scale bar: 20 µm. *n* = 8 mice per group. **(E)** Representative Western blot analysis of BAT lysates for male mice of the indicated genotypes using the indicated antibodies. **(F)** Quantification of the NDUFB8/tubulin, SDHA/tubulin, UQCRC2/tubulin, and COX4/tubulin signal ratios in E were normalized (= 1.0) to the WT controls. *n* = 4 mice per group. **(G)** Body weight of 12-wk-old male WT or FNIP1 AKO mice. *n* =8–12 mice per group. **(H–J)** Metabolic cage measurements of 16-wk-old male WT and FNIP1 AKO mice. *n* = 7–10 mice per group. Food consumption per day. **(H and I)** Locomotor activity over 12-h light/dark cycle. **(J)** Respiratory exchange rate (RER) during the light/dark cycle. Values represent mean ± SEM. *, P < 0.05; **, P < 0.01; ***, P < 0.001. P value was determined using two-tailed unpaired Student's *t*-test (A, C, F, G, and H), or two-way ANOVA and Fisher's LSD post-hoc test (H and J). Data are representative of at least two independent experiments (A–F). Source data are available for this figure: SourceData FS1.

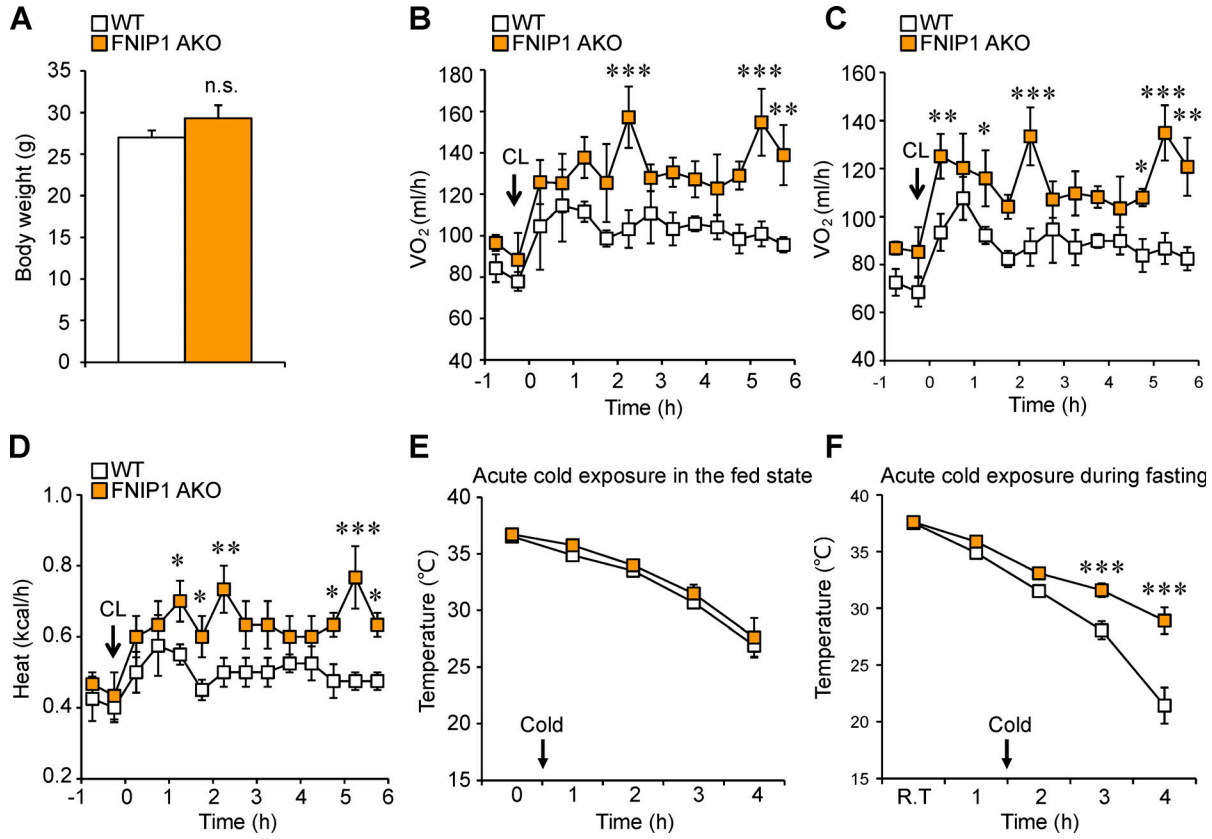

Figure S2. **Loss of adipocyte FNIP1 leads to increased respiration and cold tolerance. (A)** Body weight of indicated chow-fed 10-wk-old male mice. *n* = 3–4 mice per group. **(B–D)** Energy expenditure rates (VO_2, VCO_2, and heat production) of chow-fed 10-wk-old male mice after CL injection (0.5 mg/kg). *n* = 3–4 mice per group. **(E)** Rectal temperature recordings taken hourly during 4 h of cold exposure using a rectal digital probe in the fed state. *n* = 5–7 male mice per group. **(F)** Rectal temperature recordings taken hourly during 3 h of cold exposure using a rectal digital probe. Notably, male mice were fasted for 12 h before cold-exposure experiments. *n* = 7–8 mice per group. Values represent mean ± SEM. *, P < 0.05; **, P < 0.01; ***, P < 0.001. P value was determined using two-tailed unpaired Student's *t*-test (A), or two-way ANOVA and Fisher's LSD post-hoc test (B–F). Data are representative of three independent experiments (E).

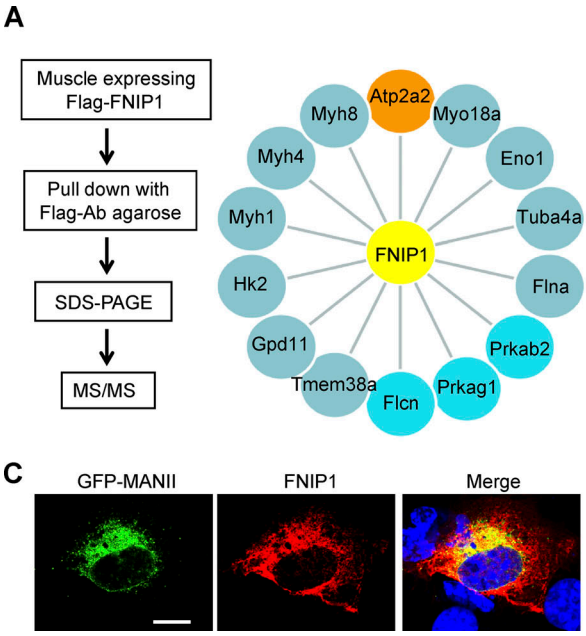

Gene	Full name	Ctrl	Flag IP
Fnip1	folliculin interacting protein 1	0	68
Atp2a2	ATPase sarcoplasmic/ endoplasmic reticulum Ca^{2+} transporting 2	0	26
Myo18a	myosin XVIIIA	0	9
Eno1	enolase 1	0	7
Tuba4a	tubulin α 4a	0	6
Flna	filamin A	0	5
Prkab2	protein kinase AMP-activated non-catalytic subunit β 2	0	4
Prkag1	protein kinase AMP-activated non-catalytic subunit γ 1	0	4
Flcn	folliculin	0	4
Tmem38a	transmembrane protein 38A	0	4

Figure S3. **Identification of SERCA binding to FNIP1. (A)** Interacting proteins of FNIP1 identified by mass spectrometry. Left: Strategy for identification of FNIP1 binding protein. Whole gastrocnemius muscle lysates from *Fnip1*^{Tg} mice were used for IP and MS studies. Right: Interacting proteins of FNIP1 (yellow) identified by mass spectrometry. The orange dots are the ER Ca^{2+}-ATPase SERCA2. The blue dots are the known binding partner of FNIP1 (FLCN, AMPKγ1, and AMPKβ2). **(B)** List of the top 10 FNIP1 binding proteins ranked by the normalized spectral abundance factor value. **(C)** Flag-FNIP1 is colocalized with the ER marker GFP-MANII in HEK293T cells. Nuclei were stained by DAPI. Scale bar: 100 µm. Data are representative of at least three independent experiments (C).

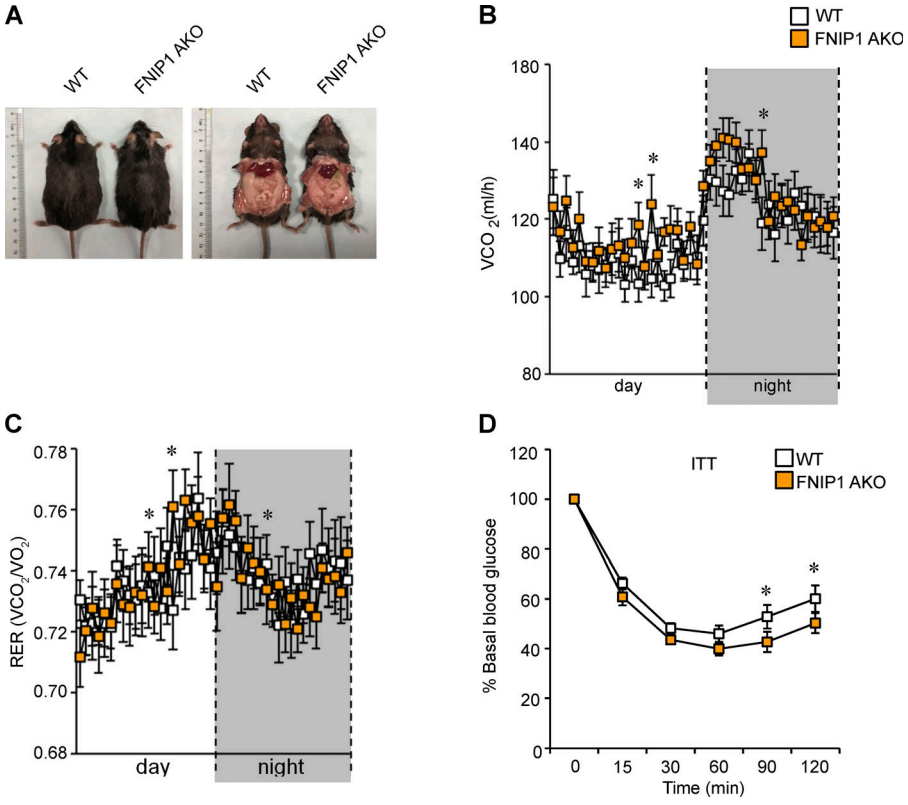

Figure S4. **Metabolic characterization of male FNIP1 AKO mice fed on a HFD. (A)** Pictures of male mice fed with HFD for 16 wk. **(B)** Carbon dioxide production per hour during the light/dark cycle. *n* = 14–15 mice per group. **(C)** Respiratory exchange rate (RER) during the light/dark cycle. *n* = 14–15 mice per group. **(D)** ITT normalized to 100% at baseline. *n* = 13–16 mice per group. Values represent mean ± SEM. *, P < 0.05. P value was determined using two-way ANOVA and Fisher's LSD post-hoc test. Data are representative of two independent experiments (A–D).

Video 1. **Real-time two-photon microscopy imaging of iWAT of GCaMP6f transgenic mice after 1 mg/kg NE stimulation.** Ca^{2+} signal was obtained by using a fluorescent filter (Excitation 410–455 nm, Dichroic FT475, and Emission 495–540 nm). Videos were obtained for 8 min at 512 × 512 resolution with a sampling interval of 10 s. Frames were taken every 10 s for 8 min.

Video 2. **Real-time imaging of white adipocytes isolated from iWAT of GCaMP6f transgenic mice after 1 µM NE stimulation.** Images were acquired every 1 s using a Zeiss LSM880 confocal microscope. The following filter Spectra was used: Excitation 470/40, Dichroic FT495, and Emission 525/50. For videos, the image sequences were saved as movies by Zeiss LSM880 (Applied Precision), and the aggregates move 30 times faster than in real time. Frames were taken every 1 s for 5 min.

Provided online are three tables. Table S1 lists genotyping and cloning primers. Table S2 lists RT-PCR primers. Table S3 lists genes up-regulated in FNIP1 AKO iWAT.